



King's Research Portal

DOI:

[10.1071/WF16178](https://doi.org/10.1071/WF16178)

Document Version

Peer reviewed version

[Link to publication record in King's Research Portal](#)

Citation for published version (APA):

Johnston, J. M., Wooster, M. J., Paugam, R., Wang, X., Lynham, T. J., & Johnston, L. M. (2017). Direct estimation of Byram's fire intensity from infrared remote sensing imagery. *INTERNATIONAL JOURNAL OF WILDLAND FIRE*, 26(8), 668-684. <https://doi.org/10.1071/WF16178>

Citing this paper

Please note that where the full-text provided on King's Research Portal is the Author Accepted Manuscript or Post-Print version this may differ from the final Published version. If citing, it is advised that you check and use the publisher's definitive version for pagination, volume/issue, and date of publication details. And where the final published version is provided on the Research Portal, if citing you are again advised to check the publisher's website for any subsequent corrections.

General rights

Copyright and moral rights for the publications made accessible in the Research Portal are retained by the authors and/or other copyright owners and it is a condition of accessing publications that users recognize and abide by the legal requirements associated with these rights.

- Users may download and print one copy of any publication from the Research Portal for the purpose of private study or research.
- You may not further distribute the material or use it for any profit-making activity or commercial gain
- You may freely distribute the URL identifying the publication in the Research Portal

Take down policy

If you believe that this document breaches copyright please contact librarypure@kcl.ac.uk providing details, and we will remove access to the work immediately and investigate your claim.

1 **Direct estimation of Byram's fire intensity from infrared remote sensing imagery**

2 *Joshua M. Johnston*^{A,B,E}, *Martin J. Wooster*^{B,C}, *Ronan Paugam*^{B,D}, *Xianli Wang*^A, *Timothy J. Lynham*^A
3 *and Lynn M. Johnston*^A

4 ^ACanadian Forest Service, Great Lakes Forestry Centre, 1219 Queen Street E, Sault Ste Marie, ON, P6A
5 2E5, Canada.

6 ^BKing's College London, Department of Geography, Strand, London WC2R 2LS, UK.

7 ^CNatural Environmental Research Council (NERC) National Centre for Earth Observation (NCEO), UK.

8 ^DCollege of Forest Resources, University of Washington, Mailbox 352100, Seattle, WA, 98195, USA.

9 ^ECorresponding author. Email: joshua.johnston@canada.ca

10 **Abstract.** Byram's fire intensity ($I_{B,tot}$; kW m⁻¹) is one the most important and widely accepted metrics for
11 quantifying wildfire behaviour. Calculation of $I_{B,tot}$ requires measurement of fuel consumption, heat of combustion
12 and rate of spread; existing methods for obtaining these measurements are either inexact or at times impossible to
13 obtain in the field. This paper presents and evaluates a series of remote sensing methods for directly deriving
14 radiative fire intensity ($I_{B,rad}$; kW m⁻¹) using the Fire Radiative Power (FRP) approach applied to thermal infrared
15 imagery of spreading vegetation fires. Comparisons between the remote sensing data and ground-sampled
16 measurements were used to evaluate the various estimates of $I_{B,tot}$, and to determine the radiative fraction ($radF$) of a
17 fire's emitted energy. Results indicate that the $I_{B,tot}$ along an advancing flame front can be reasonably estimated (and
18 agrees with traditional methods of estimation ($R^2 = 0.34-0.73$)) from appropriately collected time-series of remote
19 sensing imagery without the need for ground sampling or ancillary data. We further estimate that the $radF$ of the
20 fire's emitted energy varies between 0.15 and 0.20 depending on the method of calculation, which is similar to
21 previous estimates.

22 **Summary.** Methods for remotely measuring Byram's fire intensity with infrared cameras are developed.
23 Experimental data are collected to validate the methods. Results suggest it is possible to using infrared imager to
24 quantify fire intensity.

25 WF16178

26 J. M. Johnston et al.

27 Running header J. M. Johnston et al. / International Journal of Wildland Fire XXX (2017) XXX-XXX

28 **Introduction**

29 Wildfire behaviour is the response of a wildfire to changes in its environment in terms of spread
30 velocity, combustion rate and efficiency, flame length, direction of spread, and depth of burn. Fire
31 intensity, or fire-line intensity, is often considered the most important metric in quantifying wildfire

32 behaviour (Byram, 1959; Alexander 1982). In fire management and research, fire intensity usually refers
33 to Byram's fire intensity ($I_{B,tot}$; kW m⁻¹; Van Wagner 1965; Rothermel and Deeming 1980; Forestry
34 Canada Fire Danger Group 1992), which is the rate of energy (or heat) release per unit time per unit
35 length of the fire front (Byram 1959), and is derived from a linear combination of low heat of combustion,
36 fuel consumption and rate of spread (ROS) (Alexander 1982).

37 $I_{B,tot}$ and ROS have typically been reported together (Van Wagner 1962, 1965), and are the focus of fire
38 behaviour models (e.g. McArthur 1967; Rothermel 1972; Forestry Canada Fire Danger Group 1992). $I_{B,tot}$
39 is the conceptual basis for the Canadian Fire Weather Index, which describes the potential fire intensity of
40 a burning forest stand (Van Wagner 1974). $I_{B,tot}$ has also been used in forecasting flame lengths (e.g.
41 Butler *et al.* 2004), determining sufficient safety zones for firefighters (e.g. Butler 2014) and dictating
42 suppression tactics (Flannigan *et al.* 2009; Alexander 2013). The broad-reaching capacity of $I_{B,tot}$ to
43 describe wildfires can best be described by Van Wagner (1977) as containing 'about as much information
44 about a fire's behaviour as can be crammed into one number'.

45 $I_{B,tot}$ has been routinely calculated based on ROS, fuel consumption and heat of combustion (e.g.
46 McRae *et al.* 1979; Stocks *et al.* 2004; McRae *et al.* 2005), most of which have been applied on
47 experimental fires owing to the difficulties in obtaining fine-resolution data from larger burning areas
48 (e.g. McRae *et al.* 1979; Simard *et al.* 1984; Alexander and Lanoville 1987; Stocks 1987, 1989), where
49 traditional ground-sampling methods often are reduced to a single averaged $I_{B,tot}$ for an entire fire (e.g.
50 Stocks 1987, 1989; Alexander *et al.* 1991). Although certain remote sensing approaches have been
51 proposed (e.g. Smith and Wooster 2005) and tentatively applied (e.g. Zhukov *et al.* 2005; Dickinson *et al.*
52 2016) in estimating radiative $I_{B,tot}$ ($I_{B,rad}$), none of them have been evaluated against $I_{B,tot}$ values derived
53 from traditional ground-sampling approaches. These approaches in estimating $I_{B,rad}$ are normally based on
54 Fire Radiative Power (FRP) observations, a direct measurement of the radiant energy release rate from
55 fires. Using airborne and satellite remote sensing technologies, FRP can be assessed at landscape to
56 global scales (Kaufman *et al.* 1998; Wooster *et al.* 2003, 2005; Ichoku *et al.* 2008). The temporal
57 integration of FRP gives Fire Radiative Energy (FRE), which describes the total energy released during
58 combustion, and is generally considered proportional to the total fuel consumed (Wooster *et al.* 2005).
59 Notably, where FRP and FRE are used to describe fire energy, only the radiative fraction (*radF*) of $I_{B,tot}$ is
60 quantified, and a correction must be applied to yield actual $I_{B,tot}$.

61 Although *radF* estimates exist for stationary fires (e.g. Wooster *et al.* 2005; Freeborn *et al.* 2008) and
62 advancing flame fronts (e.g. Kremens *et al.* 2012), this fraction is not well understood with respect to $I_{B,tot}$.
63 Here, we aim to develop and evaluate remote sensing methods for estimating $I_{B,tot}$ without the need for
64 ground-sampled data, for application to very-high-resolution thermal imagery. We compare $I_{B,tot}$ with

65 three estimates of fire intensity derived from FRP- and FRE-based calculations: two are newly developed
66 in the present study and one was previously proposed (Wooster *et al.* 2004; Smith and Wooster 2005).
67 Estimates of $radF$ for each method were also derived. Two years of experimental data from a series of
68 moderate-scale burns ($\sim 35\text{-m}^2$ fuel beds) are used in this study. The data from the first year are used to
69 estimate $radF$ for each method; experimental data of the second year are used to evaluate the $I_{B,tot}$
70 prediction ability of each method.

71 **Methodology**

72 *Fire intensity estimates*

73 *Byram's fire intensity*

74 Byram (1959) proposed three different ways of measuring $I_{B,tot}$ (Eqns 1–3; Table 1), including the
75 popular Byram's Equation (Eqn 1), which is considered the universal $I_{B,tot}$ formula. Unlike Eqn 1, Eqns 2
76 and 3 have not previously been used owing to technological limitations in field sampling of E_{tot} , the
77 amount of energy released during fuel consumption (FC), and R_{tot} , the heat release rate per unit area,
78 which have now been overcome through remote sensing. For an advancing flame front, $I_{B,tot}$ is not
79 confined to the leading edge of the fire, but is emitted from the full depth of the flaming combustion zone
80 extending inward per unit length of the flame front (Fig. 1). The flame depth (Fig. 1, d and Eqn 3) varies
81 extensively with $I_{B,tot}$, ranging from a few centimetres in a low-intensity or back fire to hundreds of metres
82 in situations with extreme fire behaviour (Byram 1959). The flame depth does not include smouldering
83 (solid or glowing) combustion, which may persist for an extended period of time but does not directly
84 contribute to the intensity of the flame front (Alexander 1982). Only fuel consumed during flaming
85 combustion is considered in calculating $I_{B,tot}$ (e.g. Alexander 1982; McRae *et al.* 2005).

86 If fire spread remains in a steady state over the flame residence time (τ ; s), ROS is the flame depth over
87 τ (Eqn 4), which reveals the underlying equivalence of Eqns 1–3 in Eqn 5 (Table 1). However, FRP and
88 FRE are typically given in watts and joules as opposed to the spatially explicit FI_{rad} (kJ m^{-2}) and R_{tot} (kW
89 m^{-2}) as in Eqn 5. Here, we refer to the radiative portion of E_{tot} as FRED density (FRED, kJ m^{-2} ; Kremens
90 *et al.* 2012; Hudak *et al.* 2016), and likewise the radiative portion of the R as FRPD density (FRPD, kW m^{-2}).
91 Therefore, Eqns 2 and 3 can be adapted to incorporate FRED and FRPD termed the FRED-ROS and
92 the FRPD-Flame Depth (FRPD-FD) methods respectively.

93 *Fire Radiative Energy Density–Rate of Spread (FRED-ROS) method*

94 The FRED-ROS method adapts Eqn 2 as Eqn 6 (Table 1). To describe $I_{B,rad}$ spatially along the fire
95 perimeter, FRED is measured for each pixel along the perimeter. From a temporal perspective, FRED
96 requires enough observations to properly characterise the fluctuations in FRPD over time. Eqn 5 can then

97 be restructured as Eqn 7 (Table 1), where ROS represents the previous time step normal to the perimeter
98 (e.g. Paugam *et al.* 2013, Fig. 2a). When applied to high-resolution imagery, Eqn 7 is rasterised by
99 interpolating the time series of FRPD at each pixel and integrating over the time domain of τ . $I_{B,rad}^{FRED-ROS}$ is
100 mapped to each perimeter pixel where ROS is available for computing Eqn 6.

101 *Fire Radiative Power Density–Flame Depth (FRPD-FD) method*

102 This FRPD-based method is rooted directly in Eqn 3, with the parameters adapted as in Eqn 8 (Table
103 1), where d is the length of the normal extending from a perimeter pixel to the rear of the flame depth,
104 computed in raster cells using Pythagorean theorem scaled by the pixel resolution (Eqn 8). R_{rad} is
105 computed as the total FRPD for all pixels intersected by d at that point (Fig. 2b).

106 As in the assumptions of Eqn 5, if the flame front is in a steady state, integrating the time series of
107 FRPD at a pixel over τ (Eqn 7) is equivalent to integrating the FRPD along the depth of the flame front
108 (Eqn 8), whereas the spatial distribution of the flame depth is inherently connected through Eqn 4; thus,
109 these methods are conceptually interchangeable only during steady-state burning conditions. However, a
110 steady state is only required for Eqns 1 and 2, whereas Eqn 3 (and the FRPD-FD method) is valid in both
111 steady and unsteady conditions (Dold *et al.* 2009; Dold 2010). As such, Eqn 5 is expected to hold only
112 where a steady state exists. Therefore, Eqns 1, 2 and 3 will not always produce an identical output; in fact,
113 deviation from one another may indicate an unsteady state.

114 *Fire Radiative Power–Flame Front Length (FRP-FFL) method*

115 Smith and Wooster (2005) proposed a separate method to convert FRP into an estimate of $I_{B,rad}$
116 averaged over the flame front length (Eqn 9, Table 1, Fig. 2c).

117 *Experimental design and protocol*

118 In order to assess the ability of the three methods for estimating $I_{B,rad}$ from thermal remote sensing data,
119 we conducted 21 experimental fires during 2013 and 2014. Data collected included detailed fuel moisture,
120 heat of combustion, fuel loading and consumption measurements. Near-vertically viewing tower-mounted
121 thermal infrared imagers were deployed, and in 2014, a thermocouple grid was deployed in the fuel bed
122 for independent ROS calculation.

123 *Experimental location and burn platform layout*

124 Both experimental campaigns were conducted at the Canadian Forest Service’s Rose Experimental
125 Burn Station (near Thessalon, Ontario, Canada). At this open-air facility, a burn platform was constructed
126 at the base of a 30-m scaffold tower on which the thermal imaging cameras were mounted. To ensure that
127 no ash was lost post burn, a layer of 12 ‘fire-proof’ 1.27-cm-thick type ‘M’ marinite boards were used to

128 form the base of the burn platform, arranged into three rows of four (1.21×2.43 -m) panels (Fig. 3a, d). In
129 2014, the junction points of the panels were used for establishing a grid of 20 K-type 24-gauge (0.56-mm
130 diameter) thermocouples, with edge thermocouples inset 0.3 m into the panel to ensure flame contact
131 (Fig. 3d).

132 *Infrared imaging*

133 In 2013 and 2014, two different infrared imagers were used (Table 2). Orientation of the tower, burn
134 platform and camera positions for the moderate-scale experimental burns from which the measures of $I_{B,tot}$
135 were taken are shown in Fig. 4.

136 *Fuels*

137 All fuels in this experiment consisted of dried longleaf pine (*Pinus palustris*) needles. The uniformity
138 of the needles and their homogeneous arrangement across the burn platform permitted a high level of
139 experimental control. Fuel parameters (Table 3) were determined by direct measurement of random
140 destructive samples taken throughout the experimentation.

141 *Burn protocol*

142 The weighed fuel was loosened and evenly distributed by row of the platform (Fig. 3a). A standard
143 forestry drip torch was used to ignite the fuel beds. For all burns, ignition was conducted along the west
144 edge of the platform and consisted of a series of tightly spaced ignition lines ~ 0.5 m into the fuel bed
145 perpendicular to the edge. Given the short (7.34 m) distance available for spread, this ignition pattern
146 minimised the acceleration stage of fire growth (Fig. 3). Burns were allowed to smoulder past the stage of
147 flaming combustion; however, in all cases combustion had ended within ~ 5 min of flame front passage,
148 with minimal smouldering (owing to fuel structure and moisture). Once each burn was complete, all
149 residual ash was immediately collected and weighed by row (to prevent loss due to wind, or excessive
150 smouldering).

151 *Data collection*

152 *Data collection*

153 Fuel beds varied among burns in terms of fuel loading, fuel depth and fuel moisture content (owing to
154 atmospheric humidity; Table 4). The heat of combustion was calculated using an oxygen bomb
155 calorimeter for three randomly selected samples ranging between 0.55 and 0.76 g.

156 Once the fuel was laid out, fuel depth measurements were taken at three random locations within each
157 of the ten accessible panels along the perimeter of the burn platform, providing 30 measurements per

158 burn. Destructive fuel samples were taken within 10 min of ignition from each perimeter panel to
159 determine gravimetric moisture content (GMC, % dried mass; Table 4).

160 Thermal infrared (TIR) imaging was performed through the entirety of each burn. In 2014,
161 thermocouple outputs were logged using a series of data loggers at a rate of 2 Hz.

162 *Data processing*

163 *Estimating $I_{B,tot}$ with Eqn 1*

164 For $I_{B,tot}$ estimation, the low heat of combustion was calculated by removing the latent heat of
165 vaporisation and making reductions separately for each burn based on the fuel GMC (Alexander 1982;
166 Table 5). Fuel consumption values were computed for each burn by calculating the difference between
167 pre- and post-burn dry fuel loads (Table 5). ROS values were derived from the TIR imagery taken from
168 the fixed camera positions viewing near vertically from atop the 30-m tower (Table 5). The low heat of
169 combustion, FC and ROS values were used to compute $I_{B,tot}$ in Eqn 1 for each burn platform panel, which
170 was then generalised to describe $I_{B,tot}$ by row and by burn as required using median values.

171 *Estimating $I_{B,tot}$ with FRP, FRPD and FRED*

172 *Thermal infrared preprocessing.* In order to enable spatial measurements of ROS and flame
173 dimensions, spatially explicit data were required. All infrared imagery was georeferenced using a direct
174 linear transform (DLT; a linear remapping of pixels into a uniform planar field), with output remapped to
175 a single uniform pixel size across the full burn extent (see Pastor *et al.* 2006; Paugam *et al.* 2013).
176 Corners of the burn platform were used as ground control points (GCPs) and measured to ± 0.005 -m
177 uncertainty using a high-precision laser scanner. Prior to applying the DLT to the imagery, the pixel
178 brightness temperatures (K) were converted to spectral radiance units (Watts meter⁻² steradian⁻¹
179 micrometer⁻¹; W m⁻² sr⁻¹ μ m⁻¹) using the camera's spectral response function and the inverse Planck
180 function, because the Planck function is strongly non-linear in the mid-wave infrared (MWIR) across fire
181 temperature ranges (e.g. Wooster *et al.* 2005; Johnston *et al.* 2014). This step was necessary because
182 calculation of FRP was performed after the DLT to conserve energy during the transformation. In
183 applying the DLT, the spatial resolution of the geocorrected imagery was degraded with the new pixel
184 radiances calculated as the area-weighted average of their subpixel constituents (e.g. Dozier 1981), and
185 then the radiance values were converted back to brightness temperatures for further analysis. For all data,
186 the final uniform pixel resolution was 0.13 m.

187 *ROS calculation*

188 The approach developed by Paugam *et al.* (2013) was also used to calculate ROS from the resampled
189 TIR imagery for both the 2013 and 2014 burns. Owing to the far smaller pixel size in the present study

190 compared with that of Paugam *et al.* (2013), to maximise agreement of the TIR image-derived fire arrival
191 times at a location with those derived from the thermocouple measurements, the brightness temperature
192 (BT) threshold indicating the time of arrival was increased from the assumed 650 K (Paugam *et al.* 2013)
193 to 773 K. For the ROS calculation made using the fire arrival time map, imagery was sampled every 5–10
194 s (with higher-frequency sampling used for faster-spreading fires, Table 5). Notably, ROS is not available
195 for all perimeter pixels as the normal vector occasionally exits the burn platform in places rather than
196 intersecting another perimeter. At every level of sampling, these ROS data are typically skewed to higher
197 values (as discussed in McRae *et al.* 2005) and therefore the median values are reported by row.

198 For the 2014 burns, data from the thermocouple (TC) grid were also used to estimate fire arrival times
199 (based on a TC temperature threshold of 573 K; Wotton *et al.* 2012), supporting an independent $I_{B,tot}$
200 calculation. Arrival times were used in groups of three to compute rate and direction of spread using the
201 approach of Simard *et al.* (1984). For the final analysis, these results were generalised to the row level.

202 *FRP calculation*

203 FRP was computed using the MWIR radiance method of Wooster *et al.* (2003, 2005), with the FRP
204 factors tailored to the spectral response function of each TIR camera used as detailed in Wooster *et al.*
205 (2005). FRP was produced using the georeferenced imagery in units of Watts pixel⁻¹, and converted to
206 FRPD (kW m⁻²) as needed by multiplication by the pixel area. FRED maps in kilojoules pixel⁻¹ (and kJ
207 m⁻²) were produced by temporal integration of FRPD for each pixel.

208 *Infrared fire intensity measurement*

209 Measurement of $I_{B,rad}$ was conducted distinctly for each of the methods tested here; as a result, $I_{B,rad}$
210 values from different methods are not necessarily equivalent to one another (Table 6). For example,
211 owing to the limited fuel bed width (4.88 m), sampling FRPD along the local normal vectors for the
212 FRPD-FD method resulted in numerous vector intersections and resampling of FRPD pixels. To mitigate
213 this issue, two points were selected at opposite ends of the flame front and a single normal for each time
214 step was generated, resulting in parallel flame depth vectors.

215 *Analysis*

216 TIR and ground-sampled data from Row 1 of the burns (Fig. 3a) were not analysed because they were
217 contaminated by the drip torch fuel used for ignition. For each method, we used the 2013 dataset to
218 estimate the *radF* as the ratio of $I_{B,rad}$ to $I_{B,tot}$, but reserved the 2014 dataset for validation. Byram (1959)
219 provides an estimate of ~10–20% as general target range of *radF*. More recently, both Wooster *et al.*
220 (2005) and Freeborn *et al.* (2008) measured *radF* from laboratory-scale stationary fires as 14 and 11%
221 (respectively) when fuel moisture is considered (as it is in the results of the present study (Kremens *et al.*

222 2012; Smith *et al.* 2013)). Unlike earlier studies, Kremens *et al.* (2012) examined open-air spreading
223 flame fronts and found the $radF$ to be somewhat higher, at 17%. The difference between stationary and
224 spreading fires is significant in terms of flame front structure and the spatiotemporal distribution of
225 flaming and smouldering fuels. This difference has a significant effect on $radF$ and depends on correct
226 sampling of $I_{B,rad}$. The range suggested by Byram and the measurements of Kremens *et al.* (2012) were
227 used as reference in evaluating our results. Here, the $radF$ is an instantaneous comparison of $I_{B,rad}$ with
228 $I_{B,tot}$ and is different from other calculations that typically compare total radiant energy with total energy
229 released during combustion (e.g. Wooster *et al.* 2005; Freeborn *et al.* 2008; Kremens *et al.* 2012). The
230 2014 dataset was used further to compare the $radF$ corrected methods with the ground-sampled $I_{B,tot}$ (in
231 Eqn 10, Table 1). In both comparisons, linear regression analysis of $I_{B,rad}$ (or $I_{B,tot}$ in 2014) vs $I_{B,tot}$ was
232 used. In the direct $I_{B,tot}$ with $I_{B,tot}$ comparisons, linear regression results were examined to determine the
233 significance of their deviation from the line of perfect agreement (LPA) as in Legg *et al.* (2007); the R
234 programming language was used for all statistical analysis.

235 *Testing and determining radiative fractions*

236 *Analysis of FRP- and FRPD-based methods.* Median values of $I_{B,rad}^{FRPD-FD}$ and $I_{B,rad}^{FRP-FFL}$ for each row
237 were compared with $I_{B,tot}$ (Eqn 1), to assess each method's ability to describe $I_{B,rad}$. The fastest-moving
238 fires were not analysed because the fire reached the end of the fuel bed while the ignition line was still
239 flaming (e.g. 12 June 2013 Burn 1, and 18 June 2013 Burn 2), preventing the full flame depth from
240 developing.

241 *Analysis of FRED-ROS method.* The FRED-ROS method was not directly evaluated against $I_{B,tot}$ as
242 the ROS of Paugam *et al.* (2013) was used by both the $I_{B,tot}$ and $I_{B,rad}^{FRED-ROS}$ calculations, resulting in a lack
243 of complete independence in the data. Also, it is not desirable to sample ROS using independent methods
244 as this introduces error where the ROS outputs do not perfectly agree (e.g. Johnston 2016). However,
245 because both the FRED-ROS and Eqn 2 include ROS as a linear factor, the FRED-ROS method was
246 evaluated by comparing the remaining terms in Eqns 2 and 6.

247 *Statistical analysis of radF.* Data with respect to burn, row, ROS, FC and GMC were analysed for
248 each sample of $radF$ from the various FI_{rad} methods. For each $I_{B,rad}$ method, backward stepwise linear
249 regression analysis was performed, using all these parameters and their interactions as predictors of $radF$.
250 Additionally, mixed-effect model analysis was conducted where $I_{B,rad}$ method, ROS, FC and GMC were
251 treated as fixed effects, and burn and row were treated as random effects in predicting $radF$.

252 *Validation of $I_{B,tot}$ methods*

253 The FRPD-FD and FRED-ROS methods were evaluated using the 2014 data by applying Eqn 10 to
254 $I_{B,rad}^{FRPD-FD}$ and $I_{B,rad}^{FRED-ROS}$ and the $radF$ calculated with the 2013 data to yield complete $I_{B,tot}$, which was
255 compared with ground-sampled $I_{B,tot}$. This validation was not attempted with the FRP-FFL owing to the
256 limited success in the initial analysis (see *Results*).

257 Notably, the $radF$ (Figs 6–8) distributions range from 0.1 to 0.6; attempts to model $radF$ based on
258 additional experimental data were not significant (see *Results*). In the context of the present study, fixed
259 exemplar $radF$ were applied in an attempt to determine which fraction best suits these experimental
260 conditions.

261 The FRPD-FD method was evaluated using the derived $radF$ of 0.26 (median of the distribution in Fig
262 7d), 0.24 (the regression coefficient in Fig. 7c), and 0.17 (the value used in the FRED-ROS validation).
263 Notably, $radF$ are linear scalars of FI_{rad} , so they have no effect on R^2 or P values for each trial (Fig. 9).

264 The FRED-ROS method was evaluated using the estimated $radF$ 0.21 (median in Fig. 8), 0.17 (the
265 regression coefficient of the non-independent comparison) and 0.15 (near lower bound of the range
266 suggested by Kremens *et al.* 2012). Fig. 10 shows the results of the comparison of these data with the
267 2014 data, using the $I_{B,tot}$ produced with the IR ROS, which suffered from the same lack of independence
268 that interfered with the initial evaluation. This evaluation was then repeated using the TC ROS for $I_{B,tot}$
269 (Fig. 11).

270 **Results**

271 *FRP- and FRPD-based methods of FI_{rad} measurement*

272 The linear regression shows a significant relationship between $I_{B,tot}$ and the FRP-FFL method by row of
273 the burn platform (Fig. 6a); however, the relationship is not stronger than that of relating FRP directly to
274 $I_{B,tot}$ (Fig. 5) and it showed no advantage in predicting $I_{B,rad}$. The $radF$ of this method has a mean value of
275 ~0.10, with a broad range (Fig. 6b), indicating a lack in stability. A second iteration of this method was
276 executed with FRP limited to the flaming pixels, but showed no significant improvement (Fig. 6c, d),
277 suggesting the length measure (which is constrained by plot size) may be the limiting factor rather than
278 the FRP sample area.

279 Linear regression between $I_{B,tot}$ and the FRPD-FD method by row using the 773 K arrival and 773 K
280 flame termination thresholds showed no significance (Fig. 7a). Similarly, the $radF$ distribution is very
281 unstable (Fig. 7b). The linear regression between $I_{B,tot}$ and the FRPD-FD method by row using the 773 K

282 arrival and 700 K flame termination thresholds (Fig. 7c) is significant, and superior to that of the FRP-
283 FFL and FRP comparisons. The mean fraction derived from the *radF* distribution is 0.29 (Fig. 7d).

284 *FRED-ROS method of $I_{B,tot}$ measurement*

285 Direct comparison of the FRED-ROS method with $I_{B,tot}$ is significant ($R^2 = 0.97$, $P < 0.0001$), but
286 misleading owing to the lack of independence in ROS; however, the regression coefficient (0.17) is
287 valuable as a potential *radF* value. Alternatively, comparison of FRED with E_{tot} (from Eqn 2) is also
288 significant (Fig. 8a) and the *radF* takes on a fairly normal distribution (Fig. 8b), with a mean of 0.21 (s.d.
289 0.04).

290 *Results of statistical analysis of radF*

291 The linear regression analysis of *radF* with all predictors and their interactions for the FRED-ROS
292 method was significant (but not for the other two methods) and the backward stepwise approach
293 revealed that GMC is a weak predictor of *radF* (adj. $R^2 = 0.07$, $P = 0.04$). The mixed model analysis of
294 *radF* including method as a fixed effect and the random effects of burn and row was not significant ($P >$
295 0.05 for all predictors).

296 *Direct estimation of $I_{B,tot}$ using the 2014 dataset*

297 The FRPD-FD method was evaluated as a predictor of $I_{B,tot}$ using *radF* corrections. For the *radFs*
298 tested (0.26, 0.24 and 0.17), the regressions were significant (Fig. 9). However, the agreement was
299 somewhat weak (Fig. 9), and the deviation from the LPA was not significant for all *radFs* tested (Table
300 7). Notably, when validating the FRPD-FD method with the 0.17 *radF*, the *t*-score is negative (Table 7),
301 indicating that this model overestimates $I_{B,tot}$ (Fig. 9c), which could be attributed to an underestimation of
302 the *radF*. This suggests the ideal *radF* lies between 0.17 (c) and 0.24 (b).

303 When evaluating the FRED-ROS method as predictor of $I_{B,tot}$ with *radF* corrections, all fractions tested
304 were significant (Fig. 10). All the regressions were significant while using independent TC ROS for the
305 ground-sampled $I_{B,tot}$ in the tests (Fig. 11). As shown in Fig. 11, given the much lower R^2 (0.34), the LPA
306 remains in the 95% confidence interval (CI) for all three *radF* values, and the deviation from the LPA
307 was not significant in this case for all *radFs* tested (Table 7). Notably, the *radF* of 0.15 produces the most
308 accurate results for the FRED-ROS method where the ROS was not independently calculated (Fig. 10).
309 With the lack of specific results in comparing this method with $I_{B,tot}$ with independent ROS (where the
310 correlation is much weaker), and the certainty of the results from the comparison in Fig. 10, it is probable
311 that the *radF* of 0.15 (Fig. 10c) is best suited for the FRED-ROS method at this scale.

312 Discussion

313 This study suggests that with high-spatial-resolution TIR imagery, the FRPD-FD is superior to the
314 FRP-FFL method in estimating FI_{rad} from a single image. The major difference is that the FRPD-FD
315 method samples $I_{B,tot}$ at individual positions along the flame front (Byram 1959; Eqn 3), producing unique
316 estimates of $I_{B,rad}$ at each point, whereas the FRP-FFL method averages $I_{B,rad}$ across the full length of the
317 flame front. Both methods are quite sensitive to how the distance measures are calculated, though d
318 measurements (e.g. Fig. 12) vary significantly along the flame front, FFL offers a single value for each
319 image. The FRPD-FD method only functions when the flame depth is correctly measured (e.g. Fig. 7),
320 and the FRP-FFL method may be limited by the lack of a complete flame front length (i.e. a fire perimeter
321 that encircles the fire area) as the FRP sampling zone does not affect its performance (Fig. 6). Additional
322 assessment at larger scales is required to determine if this is indeed the limiting factor on the FRP-FFL
323 method.

324 Even without ROS, the FRED-ROS performs strongly compared with the FRP and FRPD methods.
325 The $radF$ (0.21 ± 0.04 , Fig. 8b) is similar to the upper bound proposed by Byram (1959), and overlaps
326 with that of more recent work (e.g. 0.17 ± 0.03 ; Kremens *et al.* 2012).

327 In the case of the FRED-ROS method, GMC did show borderline significance (adj. $R^2 = 0.07$, $P =$
328 0.04) in predicting $radF$. This result is in agreement with recent studies that found a connection between
329 fuel moisture and the FRP to FC relationship (e.g. Smith *et al.* 2013), and is not surprising given that low
330 heat of combustion is determined in part by GMC (Alexander 1982). It is probable that variability in $radF$
331 is better explained by parameters not tested here, such as heterogeneity of soot distribution, vertical flame
332 depth and other geometric properties, because flame emissivity is largely controlled by the depth of the
333 viewing path (Johnston *et al.* 2014).

334 In both cases, when the FRED-ROS and the FRPD-FD methods were compared with independent
335 ground-sampled $I_{B,tot}$ datasets, an R^2 of ~ 0.3 – 0.4 was observed. The relatively weak R^2 here can be partly
336 attributed to the imperfect agreement between the independent ROS methods being used ($R^2 = 0.42$ –
337 0.77). It may also be attributed to the application of Eqns 1 and 2 where the fires are periodically not in a
338 steady state (Dold *et al.* 2009; Dold 2010), which would also affect the evaluation of the FRPD-FD
339 method as it is compared with Eqn 1. That being said, in both cases, the regression coefficient of the
340 linear fit was much closer to the LPA and prediction bias was lowered when $radF$ was below 20% (lower
341 than the value estimated from the data herein). Therefore, for these data, the true $radF$ of FRP-driven $I_{B,tot}$
342 measurements may indeed fall within the range suggested by Byram (1959) of 10–20% and those
343 measured by Wooster *et al.* (2005), Freeborn *et al.* (2008) and Kremens *et al.* (2012) (~ 14 , ~ 11 and $\sim 17\%$
344 respectively).

345 A key assumption in applying these methods and in deriving the *radF* is that FRP accurately
346 characterises *radF* emissions. FRP calculations apply the Stefan–Boltzmann law to determine total
347 radiant exitance assuming that fire emissions obey Lambert’s cosine law (e.g. [Wooster et al. 2003](#)).
348 However, radiant fire energy has been found to vary with observation angle (e.g. [Freeborn et al. 2008](#);
349 [Frankman et al. 2013](#)), and as such the Lambertian assumption may not be strictly accurate. This potential
350 error has also been acknowledged in the context of measuring radiation from flame fronts ([Kremens et al.](#)
351 [2012](#)). Therefore, the *radF* found in the present study may not be identical where flame structure and
352 viewing angles differ substantially from the present conditions. A comprehensive physical model for *radF*
353 may overcome these restrictions.

354 In applying the FRED-ROS method, FRPD should only be integrated over τ to prevent the inclusion of
355 smouldering energy. This is not always practical in validation studies, as fuel consumption values
356 available from ground sampling often also include some smouldering FC ([Alexander 1982](#)).
357 Subsequently, when comparing Eqn 7 outputs with ground-sampled values, the time domain should
358 reflect the time gap before FC sampling, and when applied to describe true $I_{B,tot}$ integration should be
359 limited to τ . In this study, FRPD was integrated over the full time series; however, given the fuels and
360 experimental conditions, virtually no smouldering combustion was observed.

361 The FRED-ROS method has the advantage that it includes the most temporally unstable inputs to $I_{B,tot}$
362 (ROS) directly, providing a complete description of fire behaviour along the perimeter ([Fig. 13](#)).
363 However, this advantage also demands very high-temporal-resolution imagery, which is frequently
364 unavailable. This method is also limited by the assumption that the flame front is travelling at a steady
365 state between observations; consequently as the temporal resolution of FRPD sampling is reduced, the
366 uncertainty increases.

367 The FRPD-FD method provides an instantaneous measurement of $I_{B,tot}$ but is not limited by frequency
368 of data observations and assumptions of a steady state. However, it does lack an explicit reference to
369 ROS, which is desirable to report alongside $I_{B,tot}$ ([Van Wagner 1965](#); [Alexander 1982](#); [McRae et al.](#)
370 [2005](#)); if ROS is of interest, additional assumptions may be required to evoke Eqn 4. Eqn 8 is limited by
371 the quality of the measurement of d . Highly accurate flame depth measurements are required and it is
372 difficult to assess the effect of all potential factors (e.g. smoke plume absorption) on the temperature
373 thresholds for determining d . At the same time, for imagery with larger pixel areas, it is necessary to
374 estimate subpixel fire characteristics to implement this method (e.g. effective fire area by bispectral
375 analysis; [Dozier 1981](#); Gilgio and Kendall 2001), to estimate the depth of the flame front. The correctness
376 of such an application would be suspect until further testing is conducted.

377 **Conclusion**

378 In this study, three potential methods for estimating $I_{B,tot}$ directly from TIR imagery were evaluated.
379 This study has shown that it is possible to measure $I_{B,tot}$ on moderate scale for actively spreading flame
380 fronts at a fine resolution (0.13 m), using only TIR remote sensing. We demonstrated that Byram's *other*
381 equations (Eqns 2 and 3) are not only applicable to open-air fires, but may be more easily applied in the
382 field than Eqn 1.

383 The FRED-ROS and FRPD-FD methods successfully predicted $I_{B,tot}$ under data-rich conditions.
384 Though their functionality is not necessarily conclusive based solely on the agreement they exhibited with
385 ground-sampled data, these reservations are offset by their physical basis in Eqns 2 and 3, and under
386 steady-state conditions should be considered equally acceptable methods of estimating $I_{B,tot}$ alongside
387 Byram's Equation (Eqn 1). Our evaluation also suggests that the *radF* of these fires may be within the
388 ~10–20% range suggested by [Byram \(1959\)](#). Whether the effectiveness of these methods at larger scales
389 and whether the *radF* will remain in a similar range when flames increase in size (and therefore change
390 their optical properties) requires further investigation. The effect of increasing pixel sizes and time
391 intervals between observations also remains unknown and need to be investigated further. Additionally,
392 development of a physical model for the *radF* of $I_{B,tot}$ capable of varying with parameters such as viewing
393 angle, flame structure and optical properties may broaden applications of these methods in the future.
394 Pending further evaluation, it is possible that when used together, disagreement of the FRED-ROS and
395 FRPD-FD methods may indicate deviation from steady-state burning conditions, indicating a potential
396 hazard for fire managers.

397 **Acknowledgements**

398 The authors would like to thank John Studens, Alison Newbery, Alan Cantin, Dr Dan Thompson, Natasha Jurko, Dr
399 Bruce Main, François Gonard and Dr Mike Wotton for their assistance in the execution of the experimental burns.
400 We would like to thank Dr G. Matt Davies, Dr Rachel Gaulton and Professor Mike Flannigan for their insightful
401 comments on the early manuscript, and the reviewers for their constructive input. Critical support for this project
402 was provided by the Canadian Space Agency and the European Space Agency. Martin Wooster's work is supported
403 by the UK Natural Environmental Research Council (NERC) and NERC grant NE/J014060/1 supported some of the
404 work described herein. The NERC Geophysical Equipment Facility (NERC-GEF) is also acknowledged for loan and
405 training related to use of the terrestrial laser scanner.

406 **References**

407 <jrn>[Alexander ME \(1982\) Calculating and interpreting forest fire intensities. *Canadian Journal of Botany* 60, 349–](#)
408 [357. doi:10.1139/cjbot-60-3-349](#)</jrn>

- 409 <edb>Alexander ME (2013) Fire management applications of wildland fire behaviour knowledge. In 'Fire on Earth:
410 an Introduction'. (Eds AC Scott, DMJS Bowman, WJ Bond, SJ Pyne, ME Alexander) 373-391 (Wiley Blackwell:
411 Hoboken, NJ, USA)</edb>
- 412 <conf>Alexander ME, Lanoville RA (1987) Wildfires as a source of fire behavior data: a case study from Northwest
413 Territories, Canada. In 'Ninth Conference on Fire and Forest Meteorology', 21–24 April 1987, San Diego, CA,
414 USA. (American Meteorological Society: Boston, MA, USA)</conf>
- 415 <bok>Alexander ME, Stocks BJ, Lawson BD (1991) Fire behavior in black spruce–lichen woodland: the Porter
416 Lake project. Forestry Canada, Northwest Region, Northern Forestry Centre, Edmonton, Alberta. Information
417 Report NOR-X-310..</bok>
- 418 <jrn>Butler B (2014) Wildland fire fighter safety zones: a review of past science and summary of future needs.
419 *International Journal of Wildland Fire* **23**, 295–308. doi:10.1071/WF13021</jrn>
- 420 <jrn>Butler B, Finney M, Andrews P, Albini F (2004) A radiation-driven model for crown fire spread. *Canadian*
421 *Journal of Forest Research* **34**, 1588–1599. doi:10.1139/x04-074</jrn>
- 422 <edb>Byram GM (1959) Combustion of forest fuels. In 'Forest Fire: Control and Use'. (Ed. KP Davis) pp. 61–89.
423 (McGraw-Hill: New York, NY, USA)</edb>
- 424 <jrn>Dickinson MB, Hudak AT, Zajkowski T, Loudermill EL, Schroeder W, Ellison L, Kremens RL, Holley W,
425 Martinez O, Paxton A, Bright BC, O'Brien JJ, Hornsby B, Ichoku C, Faulring J, Gerace A, Peterson D, Mauceri J
426 (2016) Measuring radiant emissions from entire prescribed fires with ground, airborne and satellite sensors –
427 RxCADRE 2012. *International Journal of Wildland Fire* **25**, 48–61. doi:10.1071/WF15090</jrn>
- 428 <conf>Dold JW (2010) Vegetation engagement in unsteady fire spread. In 'VI International Conference on Forest
429 Fire Research', Coimbra, Portugal. (Ed. DX Viegas)</conf>
- 430 <conf>Dold JW, Zinoviev A, Leslie E (2009) Fire intensity accumulation in unsteady fireline modelling. In 'Sixth
431 Mediterranean Combustion Symposium', 7 June–12 June 2009, Corsica.</conf>
- 432 <jrn>Dozier J (1981) A method for satellite identification of surface temperature fields of subpixel resolution.
433 *Remote Sensing of Environment* **11**, 221–229. doi:10.1016/0034-4257(81)90021-3</jrn>
- 434 <jrn>Flannigan MD, Krawchuk MA, de Groot WJ, Wotton BM, Gowman LM (2009) Impacts of changing climate
435 for global wildland fire. *International Journal of Wildland Fire* **18**, 483–507. doi:10.1071/WF08187</jrn>
- 436 <other>Forestry Canada Fire Danger Group (1992) Development and structure of the Canadian Forest Fire Behavior
437 Prediction System. Forestry Canada, Science and Sustainable Development Directorate, Information Report ST-
438 X-3. (Ottawa, ON, Canada)</other>
- 439 <jrn>Frankman D, Webb BW, Butler BW, Jimenez D, Forthofer JM, Sopko P, Shannon KS, Hiers JK, Ottmar RD
440 (2013) Measurements of convective and radiative heating in wildland fires. *International Journal of Wildland*
441 *Fire* **22**, 157–167. doi:10.1071/WF11097</jrn>

- 442 <jrn>Freeborn P, Wooster MJ, Hao WM, Ryan CA, Nordgren BL, Baker SP, Ichoku C (2008) Relationships
443 between energy release, fuel mass loss, and trace gas and aerosol emissions during laboratory biomass fires.
444 *Journal of Geophysical Research* **113**, D01301. doi:10.1029/2007JD008679</jrn>
- 445 Giglio, L, Kendall, JD (2001) Application of the Dozier retrieval to wildfire characterization: a sensitivity analysis.
446 *Remote Sensing of Environment* **77**, 34-49.
- 447 <jrn>Hudak AT, Dickinson MB, Kremens RL, Bright BC, Loudermilk EL, O'Brien JJ, Hornsby B, Ottmar RD
448 (2016) Measurements relating fire radiative energy density and surface fuel consumption – RxCADRE 2011 and
449 2012. *International Journal of Wildland Fire* **25**, 25–37. doi:10.1071/WF14159</jrn>
- 450 <jrn>Ichoku C, Giglio L, Wooster MJ, Remer LA (2008) Global characterization of biomass-burning patterns using
451 satellite measurements of fire radiative energy. *Remote Sensing of Environment* **112**, 2950–2962.
452 doi:10.1016/j.rse.2008.02.009</jrn>
- 453 <bok>Johnston JM (2016) Infrared remote sensing of fire behaviour in Canadian wildland forest fuels. PhD thesis,
454 King's College London.</bok>
- 455 <jrn>Johnston JM, Wooster MJ, Lynham TJ (2014) Experimental confirmation of the MWIR and LWIR greybody
456 assumption for vegetation fire flame emissivity. *International Journal of Wildland Fire* **23**, 463–479.
457 doi:10.1071/WF12197</jrn>
- 458 <jrn>Kaufman Y, Kleidman R, King M (1998) SCAR-B fires in the tropics: properties and remote sensing from
459 EOS-MODIS. *Journal of Geophysical Research* **103**, 31955–31968. doi:10.1029/98JD02460</jrn>
- 460 <jrn>Kremens RL, Dickinson MB, Bova AS (2012) Radiant flux density, energy density, and fuel consumption in
461 mixed-oak forest surface fires. *International Journal of Wildland Fire* **21**, 722–730. doi:10.1071/WF10143</jrn>
- 462 <bok>Legg C, Davies M, Kitchen K, Marno P (2007) A fire danger rating system for vegetation fires in the UK:
463 The FireBeaters Project Phase 1 Final Report. The University of Edinburgh and The Met Office. (Edinburgh,
464 UK).</bok>
- 465 <bok>McArthur AG (1967) Fire behaviour in eucalypt forests. Commonwealth of Australia, Forestry and Timber
466 Bureau Leaflet 107. (Canberra, ACT)</bok>
- 467 <bok>McRae DJ, Alexander ME, Stocks BJ (1979) 'Measurement and Description of Fuels and Fire Behavior on
468 Prescribed Burns: a Handbook.' (Great Lakes Forest Research Centre: Sault Ste Marie, ON, Canada).</bok>
- 469 <jrn>McRae DJ, Jin J-Z, Conard SG, Sukhinin AI, Ivanova GA, Blake TW (2005) Infrared characterization of fine-
470 scale variability in behaviour of boreal forest fires. *Canadian Journal of Forest Research* **35**, 2194–2206.
471 doi:10.1139/x05-096</jrn>
- 472 <jrn>Pastor E, Àgueda A, Andrade-Cetto J, Muñoz M, Pérez Y, Planas E (2006) Computing the rate of spread of
473 linear flame fronts by thermal image processing. *Fire Safety Journal* **41**, 569–579.
474 doi:10.1016/j.firesaf.2006.05.009</jrn>

- 475 <jrn>Paugam R, Wooster MJ, Roberts G (2013) Use of handheld thermal imager data for airborne mapping of fire
476 radiative power and energy and flame front rate of spread. *IEEE Transactions on Geoscience and Remote Sensing*
477 **99**, 1–15.</jrn>
- 478 <other>Rothermel RC (1972) A mathematical model for predicting fire spread in wildland fuels. USDA Forest
479 Service, Intermountain Forest and Range Experiment Station, Research Paper INT-115. (Ogden, UT,
480 USA)</other>
- 481 <bok>Rothermel R, Deeming J (1980) Measuring and interpreting fire behavior for correlation with fire effects.
482 USDA Forest Service, Intermountain Forest and Range Experiment Station, (Ogden, UT, USA), General
483 Technical Report INT-93.</bok>
- 484 <jrn>Simard A, Eenigenburg J, Adams K, Nissen R, Jr, Deacon A (1984) A general procedure for sampling and
485 analyzing wildland fire spread. *Forest Science* **30**, 51–64.</jrn>
- 486 <jrn>Smith AMS, Wooster MJ (2005) Remote classification of head and backfire types from MODIS fire radiative
487 power and smoke plume observations. *International Journal of Wildland Fire* **14**, 249–254.
488 [doi:10.1071/WF05012](https://doi.org/10.1071/WF05012)</jrn>
- 489 <jrn>Smith AMS, Tinkham WT, Roy DP, Boschetti L, Kremens RL, Kumar SS, Sparks AM, Falkowski MJ (2013)
490 Quantification of fuel moisture effects on biomass consumed derived from fire radiative energy retrievals.
491 *Geophysical Research Letters* **40**, 6298–6302. [doi:10.1002/2013GL058232](https://doi.org/10.1002/2013GL058232)</jrn>
- 492 <jrn>Stocks BJ (1987) Fire behaviour in immature jack pine. *Canadian Journal of Forest Research* **17**, 80–86.
493 [doi:10.1139/x87-014](https://doi.org/10.1139/x87-014)</jrn>
- 494 <jrn>Stocks BJ (1989) Fire behaviour in mature jack pine. *Canadian Journal of Forest Research* **19**, 783–790.
495 [doi:10.1139/x89-119](https://doi.org/10.1139/x89-119)</jrn>
- 496 <jrn>Stocks BJ, Alexander ME, Wotton BM, Stefner CN, Flannigan MD, Taylor SW, Lavoie N, Mason JA, Hartley
497 GR, Maffey ME, Dalrymple TW, Blake TW, Cruz MG, Lanoville RA (2004) Crown fire behaviour in a northern
498 jack pine–black spruce forest. *Canadian Journal of Forest Research* **34**, 1548–1560. [doi:10.1139/x04-054](https://doi.org/10.1139/x04-054)</jrn>
- 499 <bok>Taylor SW, Pike RG, Alexander ME (1997) Field guide to the Canadian Forest Fire Behavior Prediction
500 (FBP) System. Northern Forestry Centre. (Edmonton, AB, Canada), Special Report 11.</bok>
- 501 <jrn>Van Wagner C (1962) On the value of a numerical concept of fire intensity. *Pulp & Paper magazine of*
502 *Canada, Woodland review*. **63**, 458–459.</jrn>
- 503 <eref>
- 504 <jrn>Van Wagner CE (1965) Describing forest fires – old ways and new. *Forestry Chronicle* **41(3)**, 301–305.</jrn>
- 505 <bok>Van Wagner CE (1974) Structure of the Canadian Forest Fire Weather Index. Department of the
506 Environment, Canadian Forestry Service, Publication number 1333. (Ottawa, ON, Canada)</bok>
- 507 <jrn>Van Wagner CE (1977) In readers' forum. *Fire Technology* **13**, 349–350. [doi:10.1007/BF02319734](https://doi.org/10.1007/BF02319734)</jrn>

508 <jrn>Wooster MJ, Zhukov B, Oertel D (2003) Fire radiative energy for quantitative study of biomass burning:
509 derivation from the BIRD experimental satellite and comparison to MODIS fire products. *Remote Sensing of*
510 *Environment* **86**, 83–107. doi:10.1016/S0034-3257(03)00070-1</jrn>

511 <edb>Wooster MJ, Perry G, Zhukov B, Oertel D (2004) Estimation of energy emissions, fireline intensity and
512 biomass consumption in wildland fires: a potential approach using remotely sensed fire radiative energy. In
513 ‘Spatial Modelling of the Terrestrial Environment’. (Eds R Kelly, N Drake, S Barr) 177-198 (Wiley: London,
514 UK)</edb>

515 <jrn>Wooster MJ, Roberts G, Perry GLW, Kaufman YJ (2005) Retrieval of biomass combustion rates and totals
516 from fire radiative power observations: FRP derivation and calibration relationships between biomass
517 consumption and fire radiative energy release. *Journal of Geophysical Research* **110**, D24311.
518 doi:10.1029/2005JD006318</jrn>

519 <jrn>Wotton B, Gould J, McCaw W, Cheney N, Taylor S (2012) Flame temperature and residence time of fires in
520 dry eucalypt forest. *International Journal of Wildland Fire* **21**, 270–281. doi:10.1071/WF10127</jrn>

521 <conf>Zhukov B, Oertel D, Lorenz E, Ziman Y, Csiszar I (2005) ‘Comparison of Fire Detection and Quantitative
522 Characterization by MODIS and BIRD, 31st International Symposium on remote sensing of Environment
523 Proceedings.’ June 20-24, 2005, Saint Petersburg, Russia.</conf>

524 Received 20 September 2016, accepted 10 May 2017

525
526
527
528
529
530
531
532
533
534
535
536
537
538
539
540
541
542
543
544
545
546
547
548

549
550
551
552
553
554
555
556
557
558

Table 1. Equation summary

Parameters: $I_{B,tot}$, Byram's fire intensity (kW m^{-1}); H_{tot} , low heat of combustion (kJ kg^{-1}); w , fuel consumption (kg m^{-2}); $r = \text{ROS}$, rate of spread (m s^{-1}); E_{tot} , available fuel energy (kJ m^{-2}); R_{tot} , combustion rate (kW m^{-2}); d , depth of the combustion zone (m); τ , flame residence time (s); FRP , Fire Radiative Power (kW); $FRPD$, FRP Density (kW m^{-2}); $FRED$, Fire Radiative Energy Density (kJ m^{-2}); $I_{B,rad}$, the radiative portion of $I_{B,tot}$; $I_{B,rad}^{\text{FRED-ROS}}$, $I_{B,rad}$ produced by Eqn 7; $I_{B,rad}^{\text{FRPD-FD}}$, $I_{B,rad}$ produced by Eqn 8; t , the instantaneous time step of the image; R_{rad} , the radiative portion of R_{tot} ; i , a pixel indicator along d ; Δd , distance along d subtended by one pixel (m); Δ_p , pixel resolution (m); $(\Delta x_d, \Delta y_d)$, length (pixels) of the x and y components of the flame depth vectors; $I_{B,rad}^{\text{FRP-FFL}}$, $I_{B,rad}$ produced by Eqn 9; l , length of the flame front (m); $radF$, the unitless radiative fraction

Reference	Formulation
1	$I_{B,tot} = H_{tot} w r$
2	$I_{B,tot} = E_{tot} r$
3	$I_{B,tot} = R_{tot} d$
4	$\text{ROS} = d / \tau$
5	$H_{tot} \left(\frac{\text{kJ}}{\text{kg}} \right) w \left(\frac{\text{kg}}{\text{m}^2} \right) r \left(\frac{\text{m}}{\text{s}} \right) = E_{tot} \left(\frac{\text{kJ}}{\text{m}^2} \right) r \left(\frac{\text{m}}{\text{s}} \right) = \frac{E_{tot} \left(\frac{\text{kJ}}{\text{m}^2} \right) d (\text{m})}{\tau (\text{s})} = R_{tot} \left(\frac{\text{kW}}{\text{m}^2} \right) d (\text{m})$
6	$I_{B,rad}^{\text{FRED-ROS}} = (FRED)(\text{ROS})$
7	$I_{B,rad}^{\text{FRED-ROS}} = \int_{\tau} FRPD(t) dt \text{ROS}$
8	$I_{B,rad} = R_{rad} d \rightarrow I_{B,rad}^{\text{FRPD-FD}} = \sum_i FRPD_i \Delta d = \sum_i FRPD_i \left(\Delta_p \sqrt{(\Delta x_d)^2 + (\Delta y_d)^2} \right)$
9	$I_{B,rad}^{\text{FRP-FFL}} = \frac{\sum FRP}{l}$
10	$I_{B,tot} = \frac{I_{B,rad}}{radF}$

559

Table 2. Comparison of infrared imagers used during the two separate campaigns

Data	2013	2014
Infrared imager	Agema 550	FLIR SC6703
Detector array	320 × 240	640 × 512
Spectral band	Narrow 3.9- μm filter	Narrow 3.9- μm filter

Dynamic range	473–1073 K	423–1123 K
Integration	Single	Superframing three temperature ranges
Temporal resolution	3 Hz	45 Hz (15 Hz post superframing)
Baseline spatial resolution	0.03 m	0.01 m

560 **Table 3. Fuel type specific parameters (± 1 s.d.) for longleaf pine (*Pinus palustris*), the primary fuel**
561 **used in this study**

Parameter	Mean (standard deviation)	Units	Number of samples
Surface area to volume ratio	59.95 (13.98)	cm ⁻¹	92
Density	756.44 (454.74)	kg m ⁻³	38
Mineral content	0.001 (0.001)	g mineral per g fuel	3
Heat of combustion	20.696 (0.378)	MJ kg ⁻¹	3
Low heat of Combustion	19.433–0.024 (GMC)	MJ kg ⁻¹	3

562 **Table 4. Preburn fuel bed characteristics collected for each fire in this study; gravimetric**
563 **moisture content is percentage by dry weight**

564 Standard deviations presented in parentheses

Date	Burn	Fuel load (kg m ⁻²)	Fuel depth (m)	Gravimetric moisture content (%)
7 June 2013	1	0.988 (0.028)	0.122 (0.001)	7.3 (1.2)
	2	0.972 (0.041)	0.120 (0.010)	9.4 (1.6)
9 June 2013	1	0.977 (0.018)	0.098 (0.008)	8.0 (2.5)
	12 June 2013	1	0.918 (0.048)	0.102 (0.001)
12 June 2013	2	0.911 (0.078)	0.074 (0.002)	6.3 (0.6)
	3	1.296 (0.060)	0.133 (0.002)	9.6 (1.0)
	14 June 2013	1	0.838 (0.040)	0.106 (0.003)
16 June 2013	1	0.878 (0.098)	0.114 (0.003)	11.1 (1.3)
	2	0.894 (0.056)	0.083 (0.001)	8.4 (1.4)
	3	0.878 (0.032)	0.094 (0.005)	8.7 (1.1)
18 June 2013	1	0.851 (0.022)	0.102 (0.006)	9.6 (2.2)
	2	1.282 (0.080)	0.136 (0.007)	9.0 (0.8)
	3	1.376 (0.023)	0.081 (0.007)	9.5 (1.3)
	4	0.915 (0.032)	0.080 (0.006)	10.4 (1.4)
	5	0.906 (0.059)	0.061 (0.008)	9.3 (3.3)
	6	1.347 (0.042)	0.126 (0.006)	9.7 (0.4)
	7	0.634 (0.026)	0.063 (0.003)	10.7 (0.8)
	8	1.401 (0.003)	0.153 (0.007)	8.9 (1.4)
26 Aug 2014	1	1.336 (0.012)	0.099 (0.015)	13.1 (1.1)
	3	1.120 (0.019)	0.090 (0.015)	12.0 (1.9)
27 Aug 2014	1	1.165 (0.013)	0.107 (0.013)	11.9 (1.2)
	4	1.183 (0.097)	0.085 (0.015)	13.5 (1.8)

565 **Table 5. Mean and standard deviation of fire behaviour parameters collected for each fire**
566 **conducted in this study**

567 Fire intensity class is provided using the Canadian Forest Fire Behaviour Prediction System (CFFBPS)
568 field guide intensity classes (IC) for describing fire behaviour based on $I_{B,tot}$ ranges (Taylor *et al.* 1997).
569 Standard deviations presented in parentheses

Date	Burn	Low heat of combustion (kJ kg ⁻¹)	Fuel consumption (kg m ⁻²)	Rate of spread (m s ⁻¹)	Fire intensity (kW m ⁻¹)	IC
7 June 2013	2	19 206 (38)	0.842 (0.045)	0.013 (0.022)	207.9 (361.9)	2
9 June 2013	1	19 240 (60)	0.885 (0.033)	0.013 (0.046)	235.0 (781.8)	2
12 June 2013	1	19 242 (28)	0.822 (0.042)	0.156 (0.099)	2353.6 (1566.0)	4
	2	19 280 (15)	0.758 (0.052)	0.039 (0.056)	549.4 (829.7)	3
	3	19 200 (25)	1.134 (0.047)	0.025 (0.031)	539.7 (690.2)	3
14 June 2013	1	19 290 (26)	0.767 (0.049)	0.013 (0.034)	205.9 (487.9)	2
16 June 2013	1	19 166 (33)	0.732 (0.108)	0.026 (0.046)	418.6 (692.3)	2
	2	19 231 (34)	0.803 (0.063)	0.052 (0.057)	847.4 (899.4)	3
	3	19 223 (26)	0.762 (0.006)	0.047 (0.042)	691.3 (614.7)	3
18 June 2013	1	19 201 (54)	0.799 (0.030)	0.014 (0.031)	235.6 (472.5)	2
	2	19 216 (19)	1.155 (0.102)	0.065 (0.081)	1301.6 (1792.1)	3
	3	19 204 (33)	1.248 (0.022)	0.013 (0.026)	314.7 (629.8)	2
	4	19 181 (35)	0.817 (0.027)	0.013 (0.044)	211.1 (681.3)	2
	5	19 209 (79)	0.770 (0.056)	0.013 (0.025)	207.5 (376.9)	2
	6	19 199 (10)	1.220 (0.038)	0.017 (0.033)	415.8 (784.1)	2
	7	19 174 (19)	0.582 (0.033)	0.065 (0.063)	747.3 (715.7)	3
	8	19 217 (34)	1.270 (0.027)	0.026 (0.037)	636.9 (909.0)	3
26 Aug 2014	1	19 217 (26)	1.225 (0.042)	0.073 (0.068)	1719.0 (1576.4)	3
	3	19 243 (46)	0.950 (0.060)	0.047 (0.058)	859.6 (1047.2)	3
27, Aug 2014	1	19 245 (33)	1.058 (0.092)	0.032 (0.055)	666.5 (1120.1)	3
	4	19 207 (45)	1.104 (0.125)	0.029 (0.059)	622.6 (1289.1)	3

570 **Table 6. Summary of infrared fire intensity method implementations**

571 FI_{rad} resolution describes the actual data available from each method, Output format refers to degraded
572 data used only for comparison with ground sampling. FRP-FFL, Fire Radiative Power–Flame Front
573 Length; FRPD-FD, Fire Radiative Power Density–Flame Depth; ROS, rate of spread; FRPD, FRP
574 density; FRED, fire radiative energy density

Method	Imagery requirements	Radiant energy	Sampling	Measurement	FI_{rad} resolution	Output format
FRP-FFL	Individual frames	FRP (kW pixel ⁻¹)	Summed for entire image (and also for flaming area separately)	Flame front identified by fixed threshold (773 K). Length measured from north to south on platform	Single value for each frame	Median by row
FRED-ROS	Time series	FRPD (kW m ⁻²)	Integrated over time series for each pixel	ROS computed for perimeter pixels using Paugam <i>et al.</i> (2013) and 773 K arrival threshold	Value for each pixel where ROS was computed	Median by row
FRP-FD	Individual frames	FRPD (kW m ⁻²)	Integrated along the normal extending from the perimeter into the flame depth	Flame front identified by fixed threshold (773 K). At 0.5-m spacing, flame depth is measure initiated following the normal and	Values at 0.5-m spacing along flame front	Median by row

terminated where two
 consecutive pixels fall
 below the termination
 threshold (773 and 700 K
 used)

575 **Table 7. Testing the deviation from the line of perfect agreement of regressions in Figs 9, 10 and**
 576 **11**

577 The column ‘95% CI’ indicates if the line of perfect agreement (LPA) is within (w), below (b) or above
 578 (a) the 95% confidence interval (CI); multiple values indicate partial containment within the 95% CI.

579 FRED, fire radiative energy density; FD, Flame Depth; ROS, rate of spread

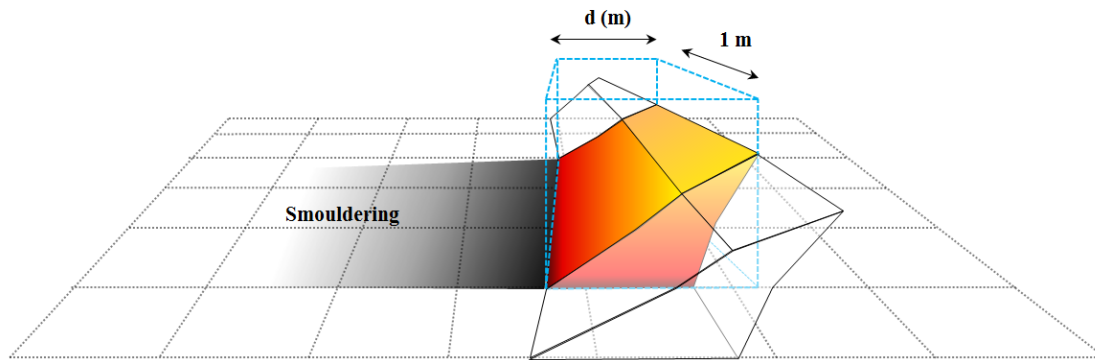
Method	Figure	Radiative fraction	R^2	slope	s.e.	Critical t	d.f. (n – 2)	t	P	95% CI
FRPD-FD	9a	0.26	0.45	0.70	0.27	2.31	8	1.11	0.299	w
FRPD-FD	9b	0.24	0.45	0.76	0.30	2.31	8	0.80	0.447	w
FRPD-FD	9c	0.17	0.45	1.06	0.42	2.31	8	-0.14	0.892	w
FRED-ROS	10a	0.21	0.91	0.68	0.04	2.06	25	8.00	<0.0001	w, a
FRED-ROS	10b	0.17	0.91	0.84	0.05	2.06	25	3.20	0.0037	w, a
FRED-ROS	10c	0.15	0.91	0.96	0.06	2.06	25	0.67	0.5090	w
FRED-ROS	11a	0.21	0.34	0.69	0.20	2.06	25	1.55	0.134	w
FRED-ROS	11b	0.17	0.34	0.85	0.24	2.06	25	0.63	0.535	w
FRED-ROS	11c	0.15	0.34	0.97	0.28	2.06	25	0.11	0.913	w

580

581

582

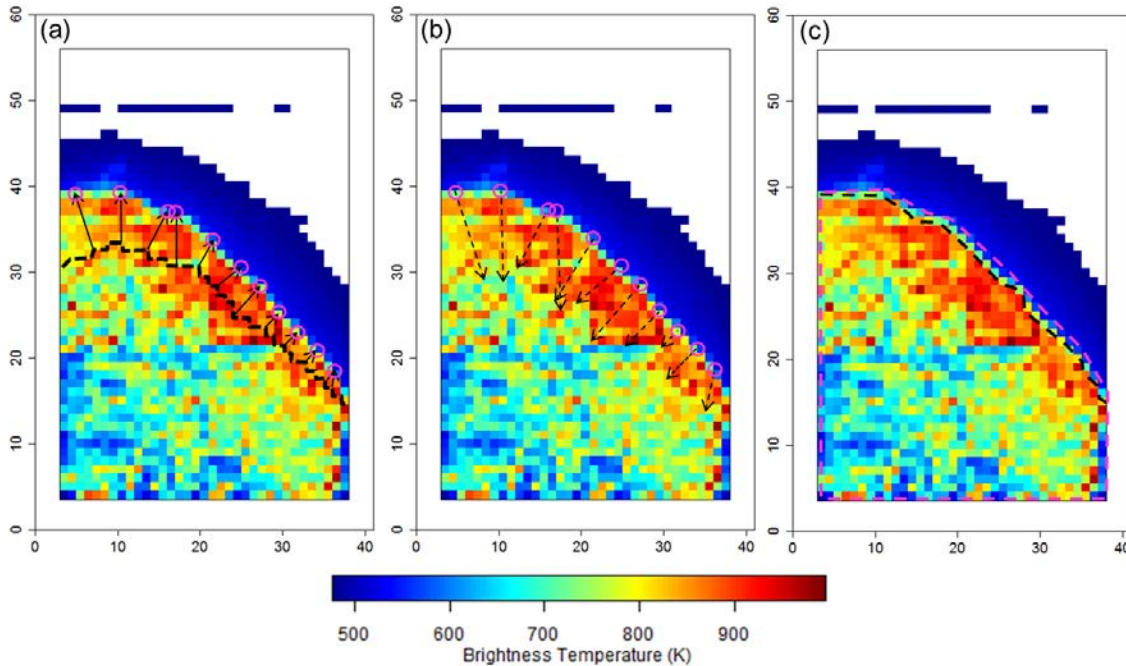
583



584

585 **Fig. 1.** Visualisation of Byram’s fire intensity ($I_{B,tot}$; kW m^{-1}) in a spreading fire. For any unit length of the flame
 586 front (m) $I_{B,tot}$ represents the energy release (kW) of the fire extending inward from the leading edge for the full
 587 depth of the active reaction zone (d ; flame depth). The energy released owing to smouldering after the fire front
 588 passage does not contribute to the intensity of the flame front, and so it is not included in the calculation of $I_{B,tot}$.

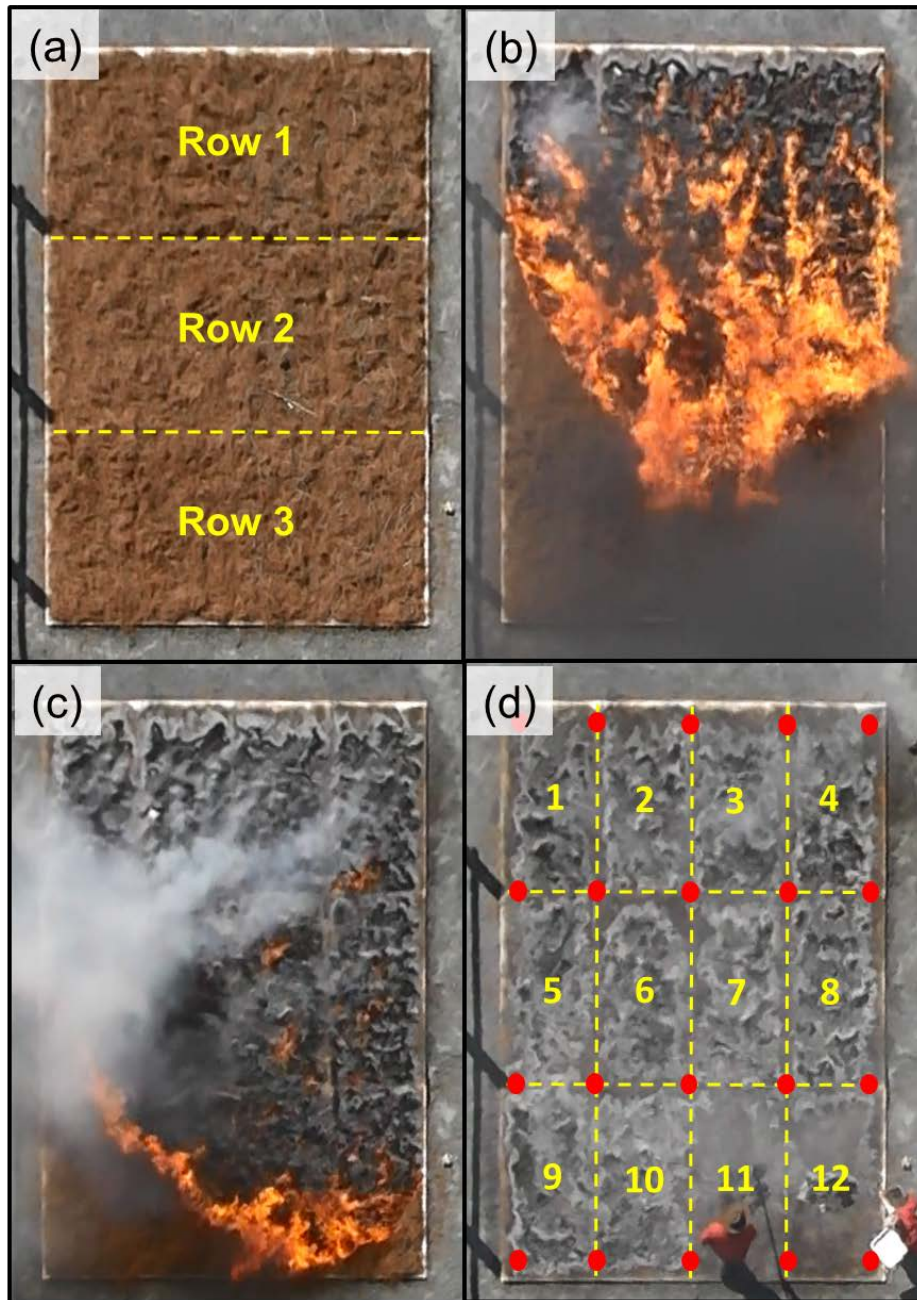
589



590

591 **Fig. 2.** Visualisation of the measurement and sampling approaches used within the different methods ((a) Fire
592 Radiative Energy Density - Rate of Spread (FRED-ROS), (b) Fire Radiative Power Density-Flame Depth (FRPD-
593 FD) and (c) Fire Radiative Power-Flame Front Length (FRP-FFL)) for calculating radiative fire intensity from
594 thermal infrared imagery applied herein. Note: sample points and vectors are illustrative and do not represent all the
595 pixels that would be sampled on the exemplar image. In (a), the FRED-ROS method integrates the measured FRPD
596 (kW m^{-2}) over the time series at each fire perimeter pixel location (pink circles) to produce FRED (kJ m^{-2}), and
597 combines this with rate of spread measured along the normal (black arrow) from the perimeter at the previous time
598 step (dotted black line) at each sample point. In (b), the FRPD-FD method sums all FRPD (kW m^{-2}) along the
599 normal (dotted black arrows) extending inward into the flame body from individual perimeter pixels (pink circles),
600 the length of these vectors is measured to determine the flame depth (FD) at each perimeter location and the FRPD
601 and FD are combined as in Eqn 8. In (c), the FRP-FFL method sums all FRP (kW) for the entire fire (outlined in
602 pink dotted line) and divides this by the measured length of the flame front (black dotted line), producing a single
603 value of radiative $I_{B, \text{tot}}$ for the entire flame front. Notably, a horizontal line of pixels is illuminated in front of the
604 flame front in this example image; this is caused by IR radiation from the fire heating an overhead cable connected
605 to other instrumentation not used in this study, artefacts such as these were masked out of analysis.

606

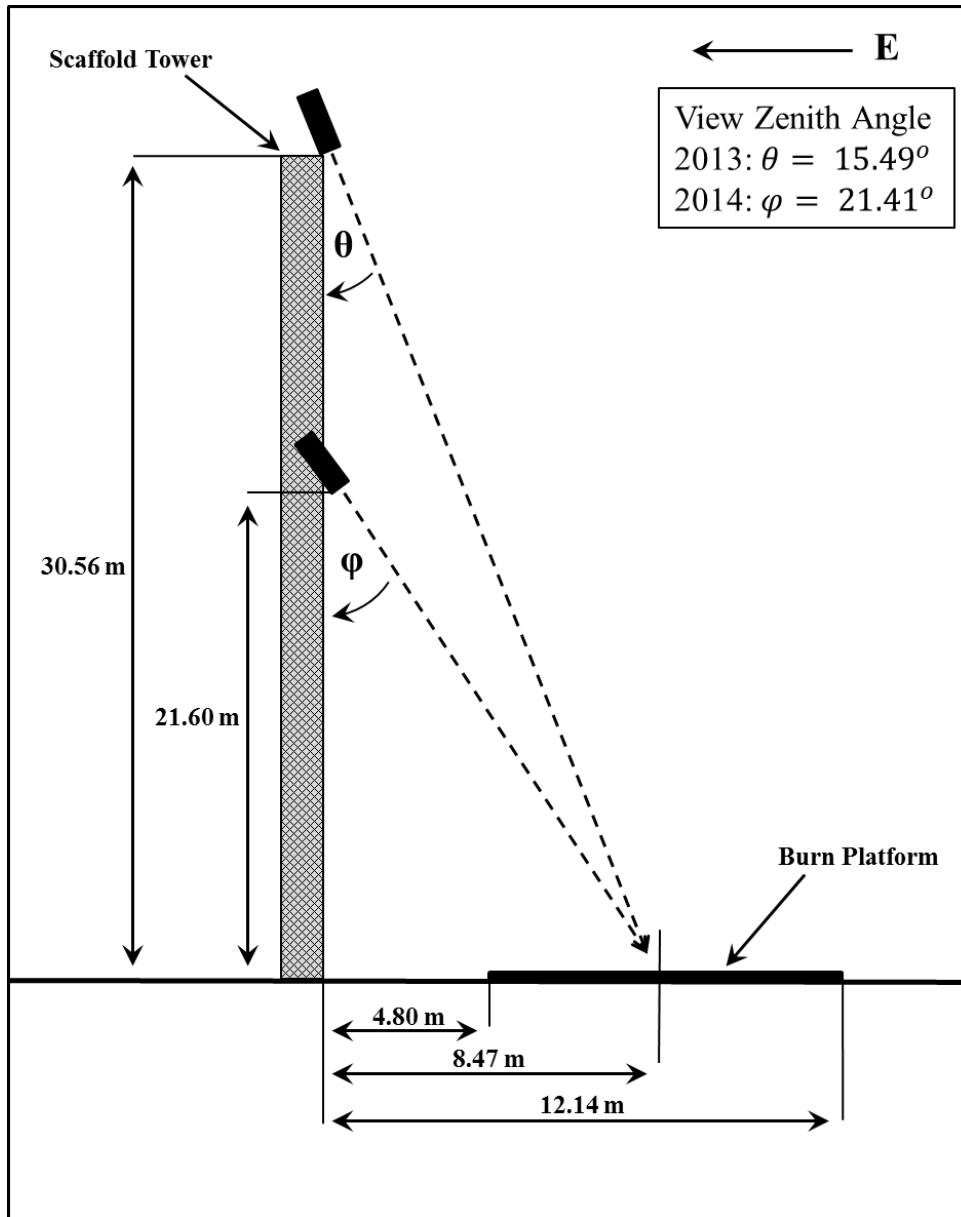


607

608 **Fig. 3.** Exemplar visible imagery of the 26 August 2014 Burn 1 experiment (Table 5), collected from camera
609 viewing from the 30-m high tower shown in Fig. 4 and taken (a) 10; (b) 50; (c) 120; and (d) 300 s after initial
610 ignition respectively. In (a), the position of the rows is identified, and the numbering of panels is found in (d). Red
611 dots in (d) indicate the location of fuel bed thermocouples used for rate of spread sampling for independent
612 comparison.

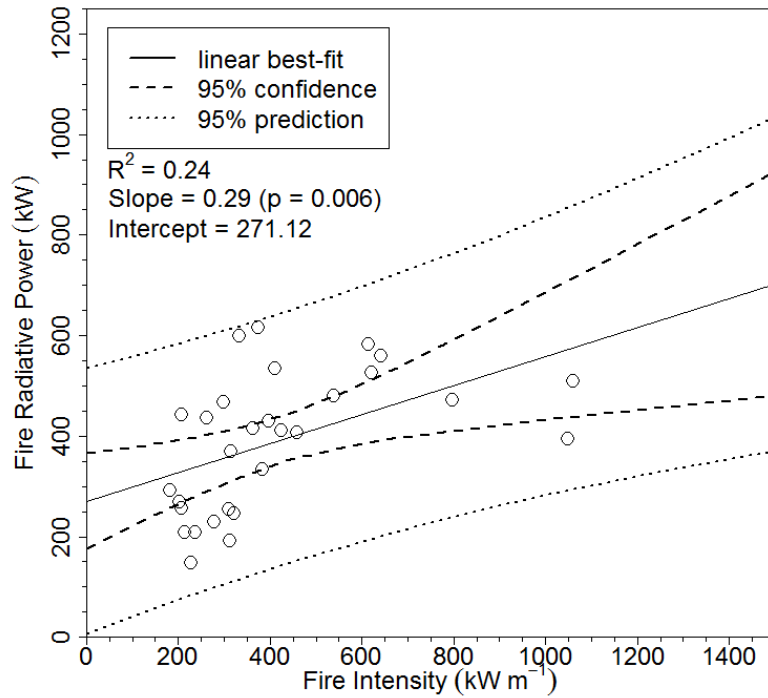
613

614



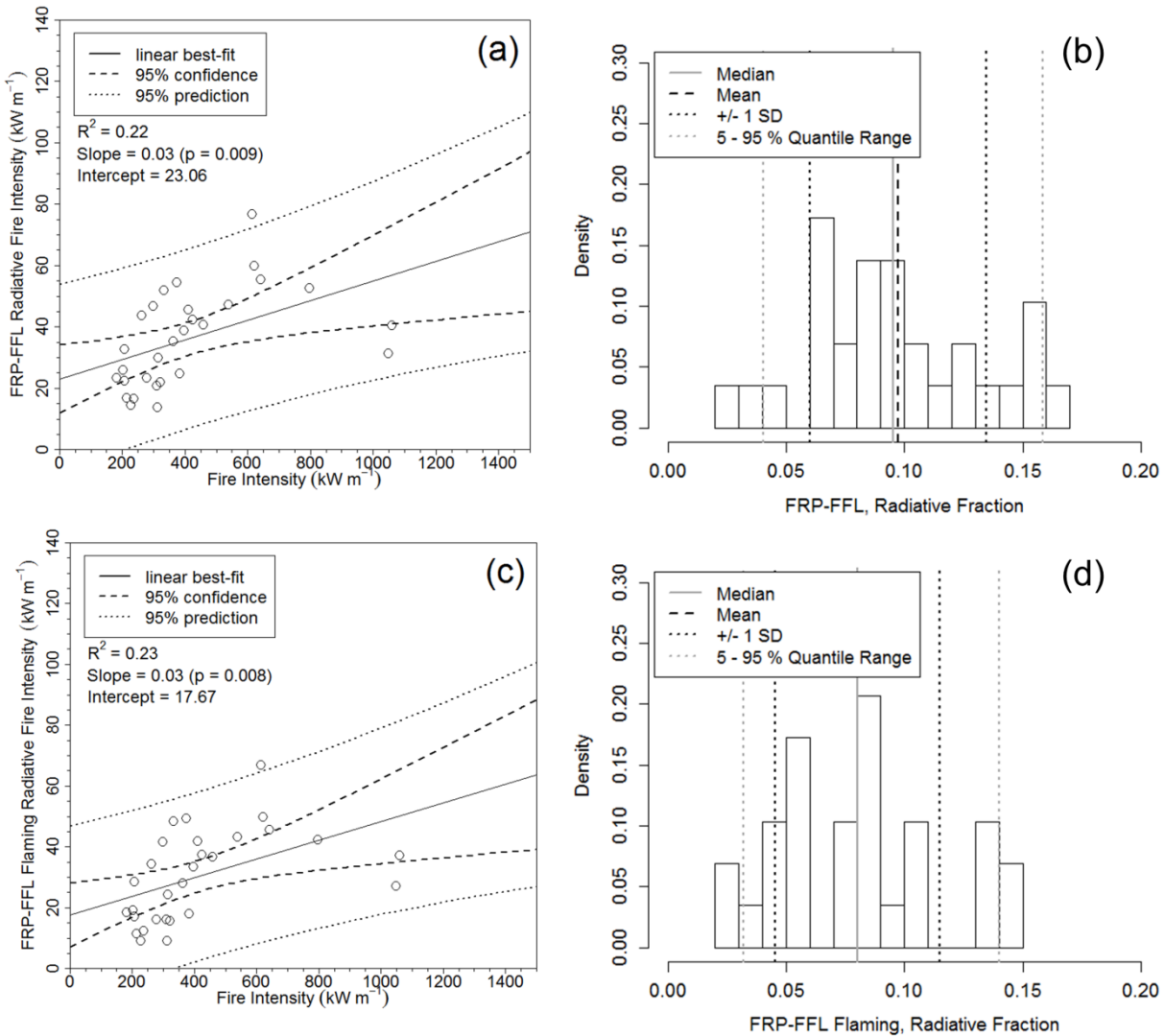
615

616 **Fig. 4.** Positioning of scaffold tower relative to the burn platform (not to scale). Placement of the mid-wave
617 infrared (MWIR) camera in 2013 and 2014 gave a view zenith angle to the centre of the burn platform of 15.49° and
618 21.41° respectively. At this range, raw spatial resolutions (averaged over the platform) were 0.035 and 0.015 m for
619 2013 and 2014 respectively.



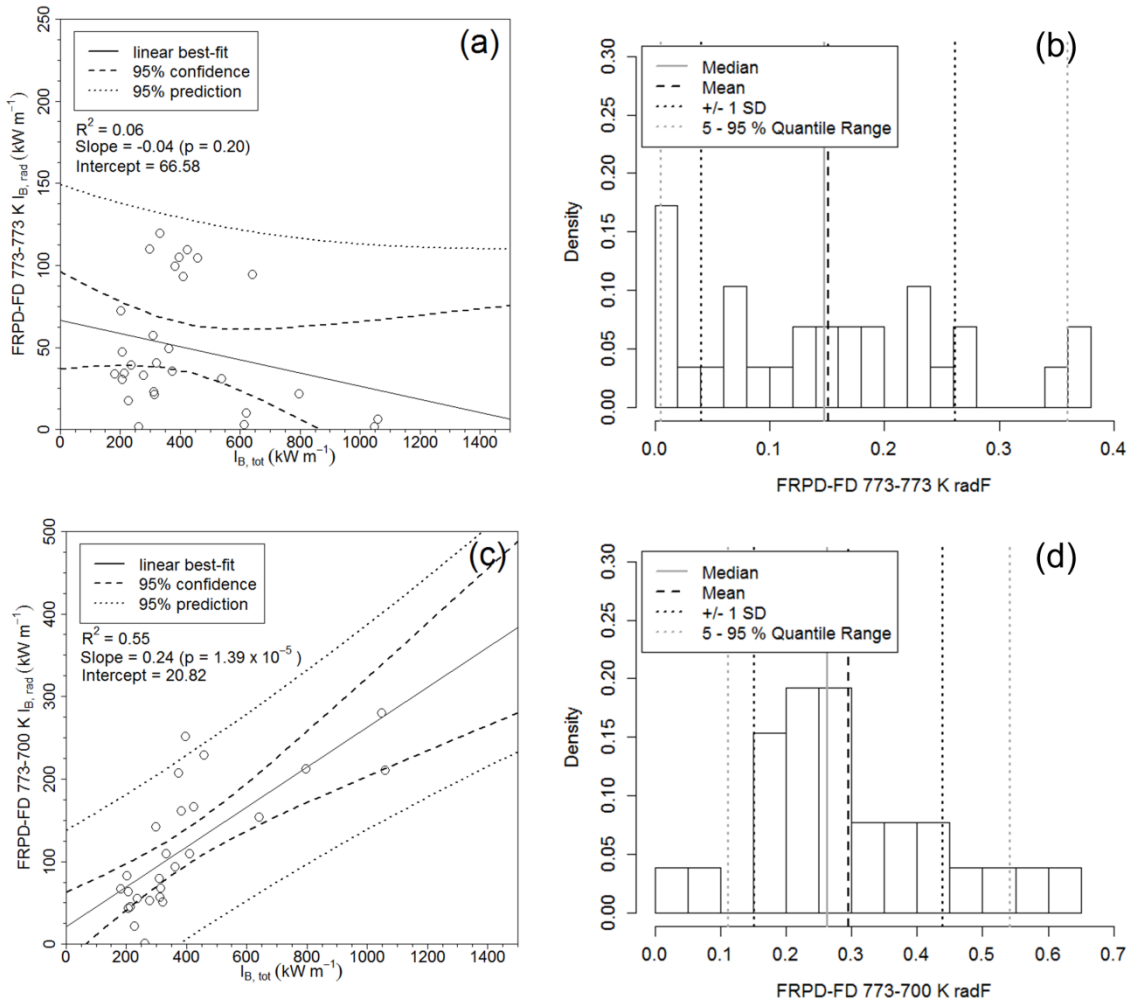
620

621 **Fig. 5.** Total Fire Radiative Power (FRP; kW) averaged by row (Fig. 3a) and compared with $I_{B,tot}$ (kW m⁻¹)
622 calculated using IR rate of spread (ROS) and Eqn 1 by row for the 2013 experimental burns (for fires which
623 contained the full depth of the reaction zone within the burn platform). Values from Row 1 were removed owing to
624 incomplete flame front presence (and therefore reduced FRP) and contamination by drip torch fuel from the ignition
625 line.



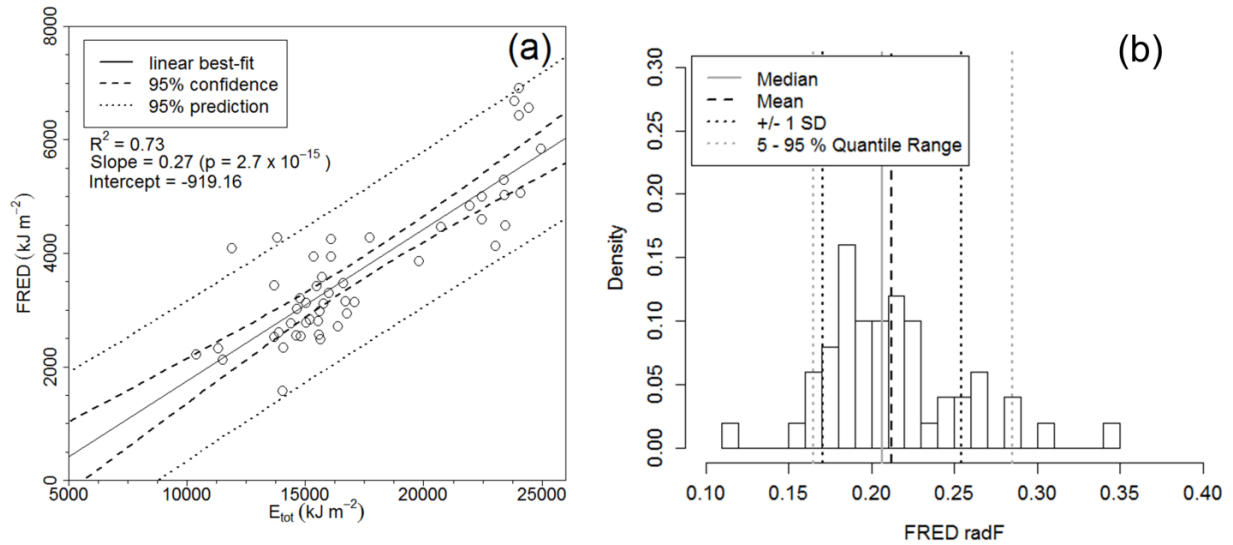
626

627 **Fig. 6.** Linear regression between $I_{B,tot}$ and $I_{B,rad}$ generated using the Fire Radiative Power-Flame Front Length
 628 (FRP-FFL) method (a), and the same method while only sampling FRP in the flaming zone (c). Frequency
 629 distribution of the radiative fractions computed by dividing $I_{B,rad}$ produced by the FRP-FFL method (b), and the
 630 same method limited to the flaming zone (d) by $I_{B,tot}$ for all data points presented in (a) and (c) respectively. The data
 631 used here were gathered using the 2013 burns and were sampled by row of the burning plot (Fig. 3a). Row 1 was
 632 removed from analysis owing to contamination with the ignition fuels and to its inability to fully represent the flame
 633 depth owing to the acceleration stage of the fire. In (b), the mean value is 0.10 with a standard deviation of 0.04, the
 634 median is 0.10, and the 5 and 95% quantile ranges are 0.04 and 0.16 respectively. In (d), the mean value is 0.08 with
 635 a standard deviation of 0.03, the median is 0.08, and the 5 and 95% quantile ranges are 0.03 and 0.14 respectively.



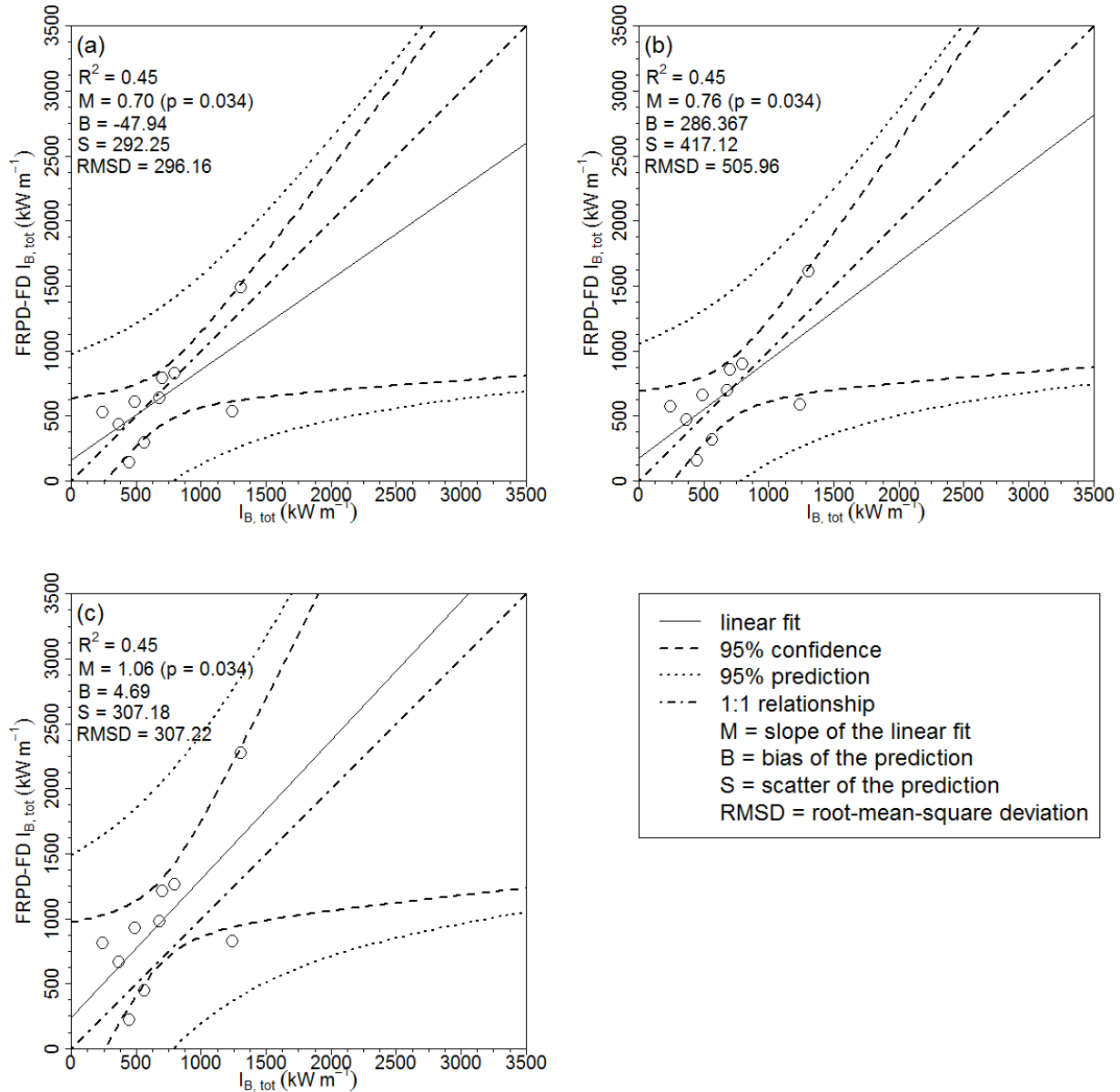
636

637 **Fig. 7.** Linear regression between $I_{B,tot}$ and $I_{B,rad}$ generated using the Fire Radiative Power Density-Flame Depth
 638 (FRPD-FD) method with a flame depth termination threshold of 773 K (a), and 700 K (c). Frequency distributions
 639 of the radiative fractions computed by dividing $I_{B,rad}$ produced by the FRPD-FD method with a flame depth
 640 termination threshold of 773 K (b), and 700 K (d) by $I_{B,tot}$ for all data points presented in (a) and (b) respectively.
 641 The data used here were gathered during the 2013 burns and sampled using medians by row of the burning plot (Fig.
 642 3a). Row 1 was removed from analysis owing to contamination with the ignition fuels and the absence of full flame
 643 depth. In (b), the mean value is 0.15 with a standard deviation of 0.11, the median is 0.14, and the 5 and 95%
 644 quantile ranges are 0.005 and 0.36 respectively. In (d), the mean value is 0.29 with a standard deviation of 0.14, the
 645 median is 0.26, and the 5 and 95% quantile ranges are 0.11 and 0.54 respectively.



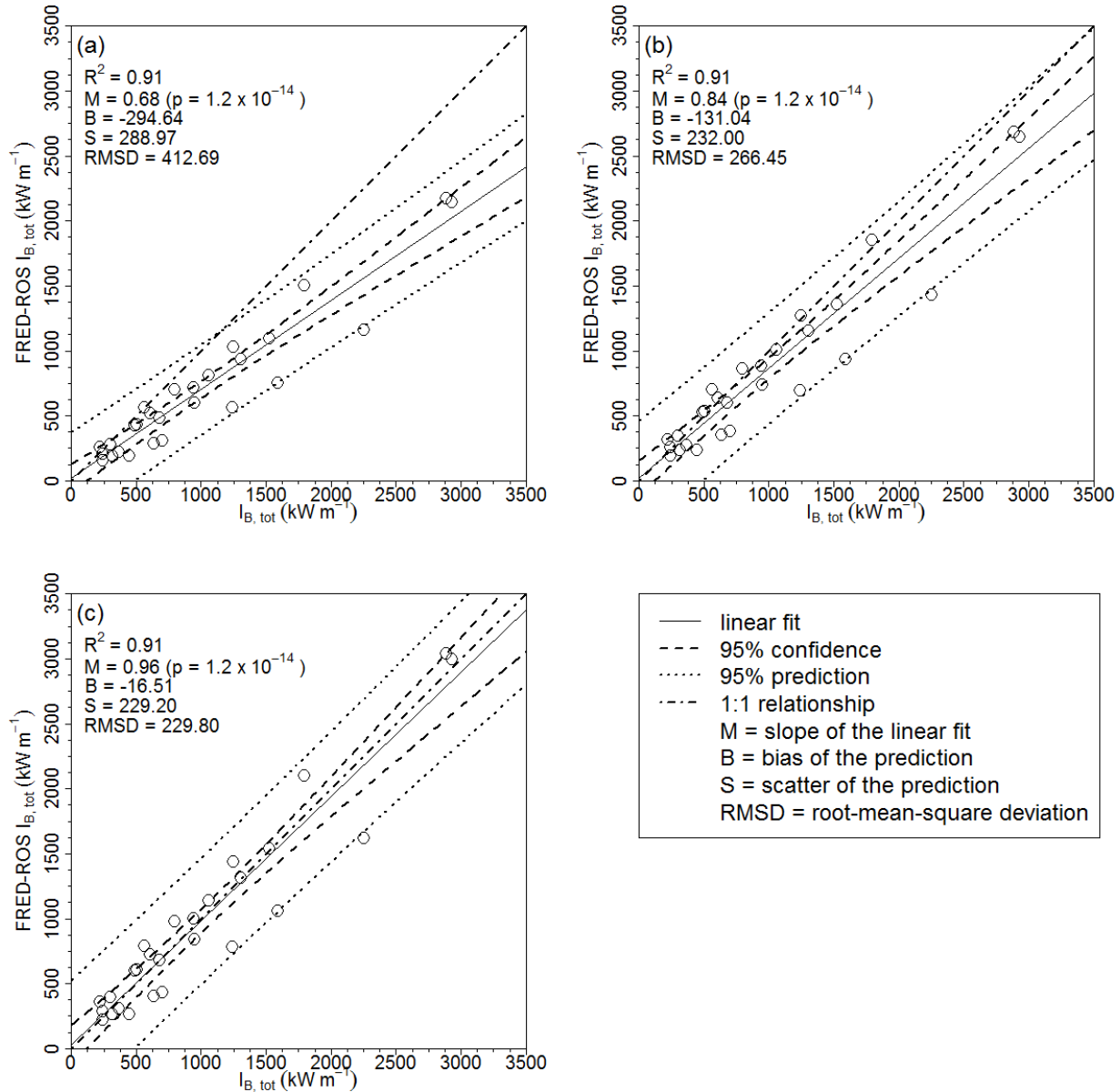
646

647 **Fig. 8.** Linear regression between the ground-sampled available fuel energy (E_{tot} ; kJ m^{-2}) and the Fire Radiative
 648 Energy Density (FRED; kJ m^{-2}) measured in the Fire Radiative Energy Density - Rate of Spread (FRED-ROS)
 649 method (a). Frequency distribution of the radiative fractions computed by dividing FRED (kJ m^{-2}) produced by the
 650 FRED-ROS method by the E_{tot} of $I_{B,tot}$ (b) for all data points presented in (a). The data used here were gathered
 651 using the 2013 burns and are presented as mean value of pixel FRED and ground-sampled low heat of combustion
 652 scaled by fuel consumption for each row to produce E_{tot} . Row 1 was removed from analysis owing to contamination
 653 with the ignition fuels. In (b), the mean value observed here is 0.21 with standard deviation of 0.04, the median is
 654 0.20, and the 5 and 95% quantile ranges are 0.16 and 0.28 respectively.



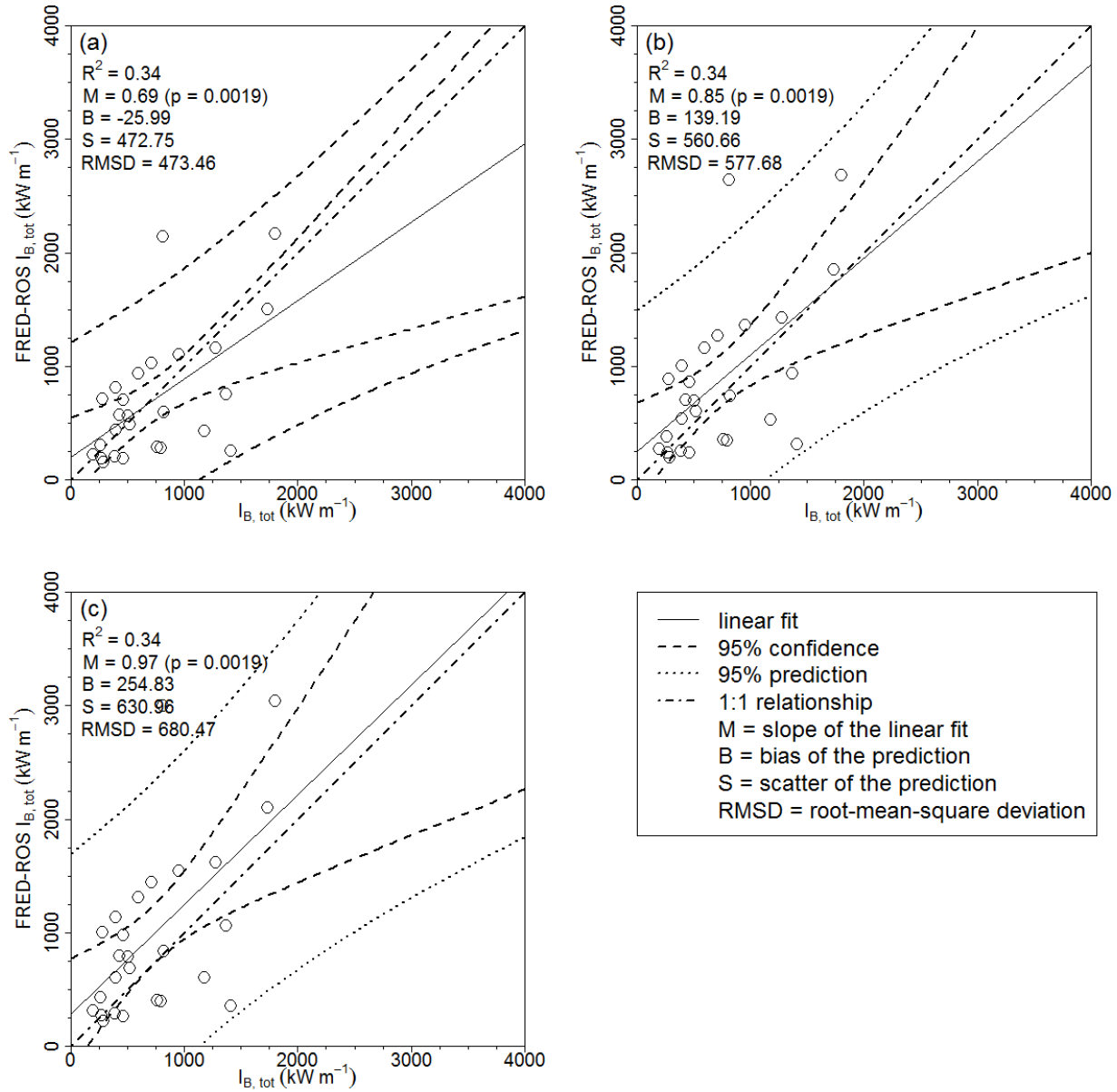
655

656 **Fig. 9.** Linear regression between $I_{B,tot}$ and $I_{B,tot}$ generated using the FRPD-FD method with three different
 657 radiative fraction corrections; (a) 0.26; (b) 0.24; and (c) 0.17. The intent of this comparison is to identify which
 658 radiative fraction best approximates the line of perfect agreement (LPA; Table 7). The data used here were gathered
 659 from the 2014 burns and were sampled using median values for each by panel. Row 1 was removed from analysis
 660 owing to contamination with the ignition fuels, panels were removed from analysis if it was not possible to calculate
 661 $I_{B,tot}$ using this method (e.g. inability to measure flame depth owing to it reaching a platform boundary).



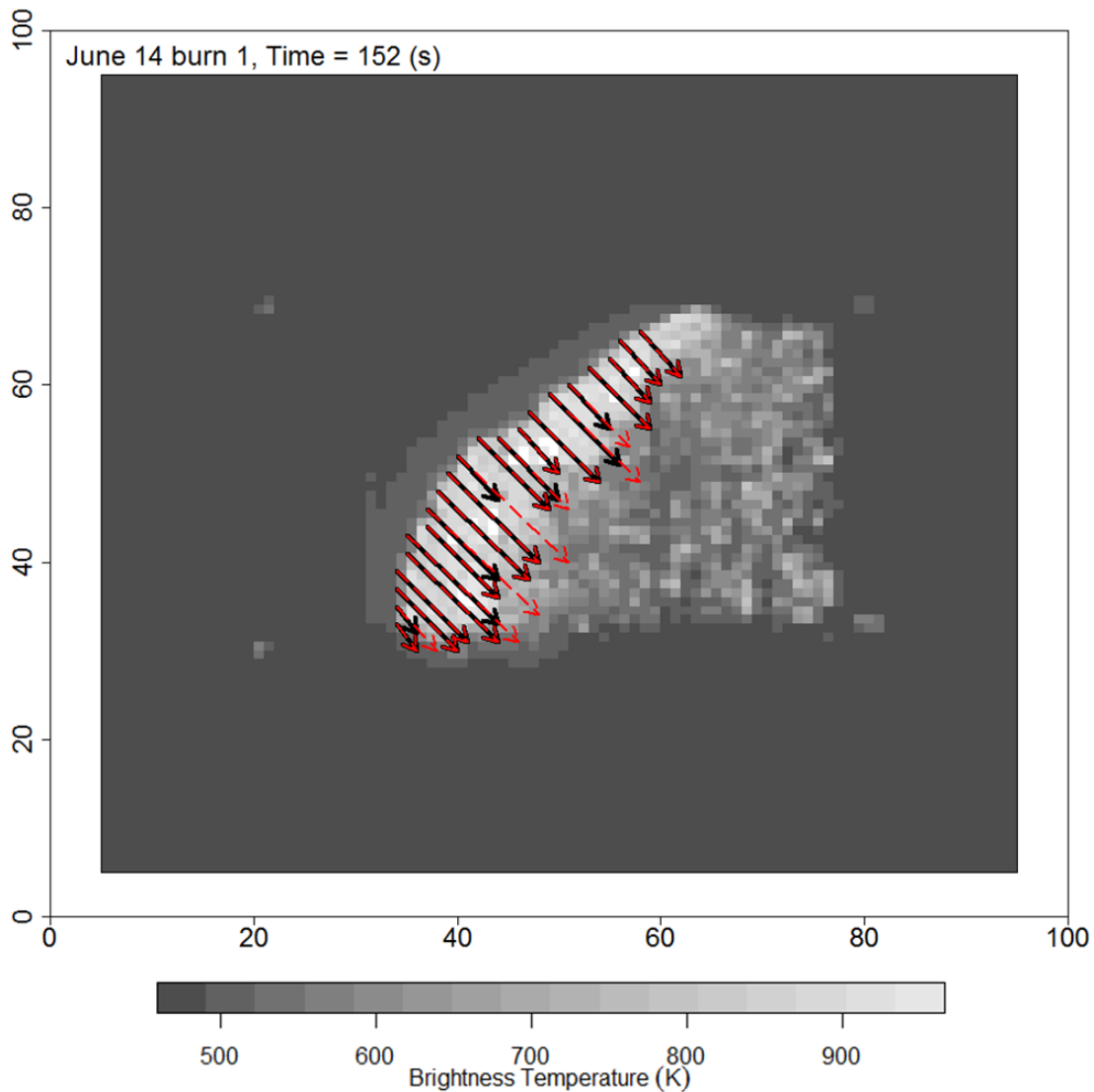
662

663 **Fig. 10.** Linear regression between $I_{B,tot}$ and $I_{B,tot}$ generated using the FRED-ROS method with three different
 664 radiative fraction corrections; (a) 0.21; (b) 0.17; and (c) 0.15. ROS used for $I_{B,tot}$ and the FRED-ROS $I_{B,tot}$ are not
 665 independent, resulting in the strong agreement found here. The intent of this comparison is not to assess this
 666 agreement, but rather to identify which radiative fraction best approximates the line of perfect agreement (LPA;
 667 Table 7). The data used here were gathered using the 2014 burns and sampled using median values for each by row.
 668 Row 1 was removed from analysis owing to contamination with the ignition fuels.



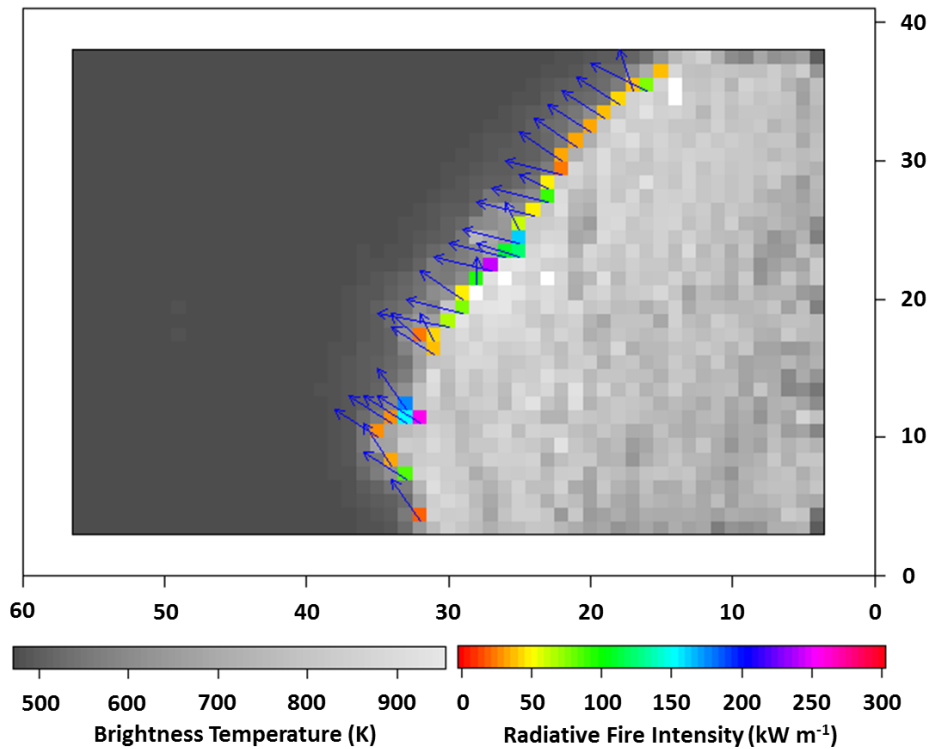
669

670 **Fig. 11.** Linear regression between $I_{B,tot}$ calculated with an independent ROS measurement method (thermocouple
 671 grid ROS) and $I_{B,tot}$ generated using the FRED-ROS method with three different radiative fraction corrections; (a)
 672 0.21; (b) 0.17; and (c) 0.15. The intent of this comparison is to identify which radiative fraction best approximates
 673 the line of perfect agreement (LPA; Table 7). The data used here were gathered using the 2014 burns and sampled
 674 using median values for each panel. Row 1 was removed from analysis owing to contamination with the ignition
 675 fuels.



676

677 **Fig. 12.** Flame depth vectors estimated using the FRPD-FD method and a flame depth termination threshold
678 temperature of 773 K (black arrows) and 700 K (red dotted arrows) on the 14 June 2013 Burn 1 of the 2013
679 experimental campaign (Table 5), 152 s after fire ignition. Data collected with the Agema 550 thermal imager from
680 a distance of 30.9 m, with the brightness temperatures shown calculated using a unitary atmospheric transmissivity
681 and emissivity. As can be seen where the temperature threshold is higher (black arrows), on occasion, this
682 measurement stops early when there is some flame depth remaining to be measured, whereas the lower threshold
683 (red dotted arrows) allows the flaming zone (area of increased brightness temperature adjacent to the leading edge of
684 the fire) to be sampled and occasionally allows the measurement to continue into the non-flaming zone (area of
685 cooler brightness temperatures that trails behind the flame front and remains above ambient background
686 temperature).



688

Fig. 13. Depiction of outputs from the Fire Radiative Energy Density - Rate of Spread (FRED-ROS) calculation of $I_{B,rad}$. The georeferenced infrared imagery is used to calculate FRPD (kW m^{-2}) at each time step and is integrated at each pixel to produce FRED (kJ m^{-2}). The infrared time series is also employed for calculation of ROS and direction of spread (blue arrows) at each time step. The FRED and ROS values are then combined at each point along the flame front to produce the FI_{rad} spatially wherever the ROS method produces measurements (coloured pixels).

^ALinear regression of the Fire Radiative Power-Flame Front Length (FRP-FFL) and Fire Radiative Power Density-Flame Depth (FRPD-FD) methods were not significant (adj. $R^2 = 0.39$ and 0.17 , $P = 0.08$ and 0.69 respectively), so the stepwise approach was not used for those two methods.

695